A Study of Transient Heat Conduction and Thermal Noise in an Earth Radiation Budget Radiometer

by

Max Savransky

Thesis submitted to the Faculty of the

Virginia Polytechnic Institute and State University

in partial fulfillment of the requirements for the degree of

Master of Science

in

Mechanical Engineering

APPROVED:

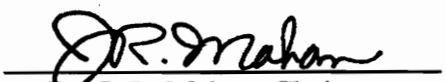

Dr. J. R. Mahan, Chairman

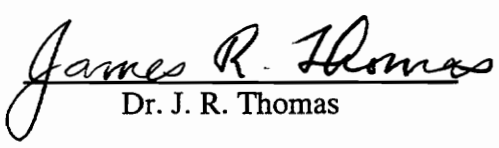

Dr. J. R. Thomas

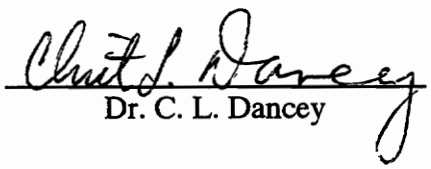

Dr. C. L. Dancey

December, 1996

Blacksburg, Virginia

Keywords: Earth, Radiation, CERES, Scanner

A Study of Transient Heat Conduction and Thermal Noise

in an Earth Radiation Budget Radiometer

by

Max Savransky

J. Robert Mahan, Chairman

(ABSTRACT)

The suite of three Clouds and Earth's Radiative Energy System (CERES) radiometers measure the radiation reflected from and emitted by the Earth from Earth orbit. The instruments are based on a two-mirror reflecting telescope which focuses incident radiation on a thermistor bolometer thermal radiation detector. The CERES radiometers scan back and forth across the Earth and surrounding space as the satellite orbits the Earth. Each scan has a period of about six seconds. This not only results in a transient radiation signal arriving at the detector surface from the scene, but also in temperature transients in the instrument structure. The instrument "zero" is obtained during the "space look" when it views cold space at each end of the scan. Some of the surfaces of the instrument structure are visible from the detector, either directly or through reflections. As a result, the radiation emitted by these surfaces will reach the detector. This form of radiation is called *thermal noise* and is undesirable. In order to determine whether the thermal noise is significant to cause concern, the transient response and temperature variations of the various components of the instrument must be known. The transient response is determined from observing the temporal variation of the temperature

distribution within the instrument structure. Since the instrument orbits the Earth, both the Earth and space make up the environment of the instrument. This means that the temperature distributions for both the space look and Earth scene must be studied. Pseudo time constants were determined from the transient space-look temperatures. The transient thermal noise was then determined from the pseudo time constants and the steady-state space-look and earth-scene temperatures. The thermal noise was shown to vary with magnitude on the order of nanowatts. This means that the thermal noise is not sufficiently large to be of concern.

Acknowledgements

I would like to thank my advisor, Dr. J. R. Mahan, for his patience and support. His professional attitude and motivation for research provided me with a challenging research problem and a relaxing environment. Dr. Mahan showed a lot of confidence in my abilities by making every effort to provide me with financial assistance for my research. I would like to thank Radiation Sciences Branch of the Atmospheric Sciences Division of NASA's Langley Research Center for their partial support of this work under Grant NAG1-1640. I would also like to thank Dr. J. R. Thomas and Dr. C. L. Dancey for their willingness to serve on my committee.

Thanks are extended to my lab colleagues Tai Nguyen, Kory Priestly, Pierre Villenueve, and Martial Haeffelin for their willingness to help. Through various group discussions, many questions were answered.

Finally, I would like to thank my family for their support and for always being there for me.

Table of Contents

List of Tables

List of Figures

1.0 Introduction

1.1 The Earth Radiation Budget

The climate is ultimately controlled by the Earth's radiation budget. Therefore, the Earth's radiation budget must be analyzed accurately in order to predict long-term weather patterns [1]. The Earth's radiation budget is made up of three components: the incident solar radiation upon the Earth, the reflected solar radiation, and the emitted longwave solar radiation. The Earth's radiation budget is defined as the difference between the incident and the sum of the emitted and solar-reflected energy streams. The components of the Earth's radiation budget may be seen in figure 1. The Earth is in

radiative equilibrium whenever this difference is equal to zero. An infinite manifold of values of the individual components of the Earth radiation budget exists corresponding to a balanced condition due to the large number of possibilities for temporal and spatial variations. The scientists' goal of Earth radiation budget research is to understand the relationships between these variations and the weather and climate. The National Aeronautics and Space Administration (NASA) is collaborating with the space agencies of other nations in developing the Earth Observing System (EOS). EOS is a consolidation of instruments and space platforms which can monitor the parameters related to climatic changes over a long time period [3].

1.2 Pre-Satellite Era Research

The importance of radiation to weather and climate patterns was recognized by many scientists prior to the development of satellites. An attempt to compute the radiative components was made by incorporating climatological data with radiative transfer models. Since computers were unavailable at that time, both the climatological data and the radiative transfer models applicable during that time period would be considered insufficient today. However, the investigations provided scientists with a relatively deep insight into the nature of the Earth's radiation budget [4]. Research on the Earth radiation budget dates back to 1917 (Dines [5]), and to Simpson in 1928 [6]. London's [7]

empirically based theoretical work in 1957 stands out in the science of the Earth's radiation budget. Scientists later discovered that the only way to obtain sufficient measurements to satisfy the coverage and sampling requirements for each of the components of the Earth's radiation budget was via satellite [4].

1.3 Satellite Missions

Initial space-based observations of the Earth's weather patterns were obtained by sub-orbital rockets in the late 1940's. In 1959, Explorer 6 made the first measurements of the Earth radiation budget components via satellite. Explorer 7 and the Television Infrared Observational Satellites (TIROS) were among the other satellites contributing to the data acquisition of the Earth radiation budget components [8]. In June 1970, the Earth Radiation Budget (ERB) experiment was selected by NASA to fly on Nimbus-6 in order to obtain data for regional and seasonal variations in the reception and re-emission of energy back into space by the Earth's climate system. The energy absorbed by the Earth's climate system is in the shortwave range (0.1 to 5.0 μm) while the re-emitted energy is in the longwave range (5.0 to 100 μm). The first of two ERB instrument packages was launched in June of 1975 on Nimbus-6 and gathered useful data from July 1975 to June 1978. The second instrument flew on the Nimbus-7 climate observatory satellite after some adjustments. Data collection began on November 16, 1978, and ended in early

1993. Most regions of the Earth are viewed once during daylight and once at night every day. While solar measurements obtained from Nimbus-6 were useless due to undetermined calibration drifts, measurements obtained from the cavity radiometer, channel 10c, on *Nimbus-7* for 14 years were very accurate. Several important results were obtained by the Nimbus ERB program from studying, for the first time, the solar variability over a complete solar cycle and in mapping both seasonal and interannual Earth radiation budget variations. The Nimbus-7 led to investigations of cloud interactions and the radiation budget [9]. The need for better accuracy led to a new satellite program.

The Earth Radiation Budget Experiment (ERBE) was initiated in 1975 with a workshop at the National Center for Atmospheric Research in Boulder, CO. It is the first multi-satellite instrument package to measure the components of the Earth radiation budget. Measurement accuracy and spatial and temporal coverage specifications were provided by The National Academy of Sciences after a review of the NASA radiation budget program. An agreement on the instrument design was reached between the National Oceanic and Atmospheric Administration (NOAA) and various university and industry representatives. In 1979, ERBE was approved as a NASA program by the United States Congress. The ERBE instrument was carried by a NASA satellite and two NOAA satellites during the mid-1980's. Each satellite carried scanner and nonscanner packages containing a complete, traceable system for inflight calibration. The nonscanner package has a solar monitor and four Earth-viewing channels. The scanning package

consists of three radiometers which scan the Earth perpendicular to the orbital track [10]. The three scanning radiometers cover different wavelength intervals. The total channel measures radiation between 0.2 and 50 μm, the longwave channel is sensitive between 5 and 50 μm, and the shortwave channel measures between 0.2 and 5 μm [7]. A pixel-by-pixel process for the scanner data and a numerical filter for the nonscanner were used to bring data from the satellite radiometers to the top of the atmosphere. After the measurements are brought to the top of the atmosphere, a time average of all the data is obtained to produce monthly averages which determine meteorological and albedo variations with solar zenith angle. These instruments and processes provide a substantial measurement accuracy [10]. The ERBE mission confirmed the influence of clouds on the regional and global Earth radiation budget. Initially, it was believed that clouds were responsible for cooling and heating the Earth. The cooling effect was due to reflection of incoming solar radiation, and the warming effect was due to absorption of outgoing thermal radiation which slowed down the cooling of the atmosphere. After a thorough analysis of the data, it was confirmed that the cooling effect was much greater than the warming postulated by the "greenhouse effect" [11]. This net cooling effect is known as Cloud Radiative Forcing. Despite the fact that the net cooling effect of clouds on the Earth has been determined, clouds are still one of the largest uncertainties in our understanding of the climate. In order to provide more insight into their behavior, a new measurement program has been established to continue where ERBE left off [12].

The Clouds and The Earth's Radiant Energy System (CERES) radiometers will replace ERBE. The goals of CERES are to give more insight into the effect of clouds on the Earth's climate, improve inputs into atmospheric models, and provide extended weather forecasts. The CERES radiometers contain flight calibration systems, detectors, and other systems (axis drive mechanisms, electronics, thermal control materials and headers, etc.) pertinent to the instrument. The CERES scanning module is shown in figure 2. The instrument initiates its scan with a spatial profile for about 0.4 seconds. The instrument then rotates to view the Earth for about 2.5 seconds, then back to space for about 0.2 seconds, and then it is calibrated for about 0.2 seconds by the Internal Calibration Module (ICM). It then rotates to view space for about 0.2 seconds, the Earth for 2.5 seconds and back to space for 0.4 seconds. The total time for the scan is approximately 6.4 seconds. The CERES scanning profile is shown in figure 3. The currently planned rate of rotation is six angular degrees per second, but it can be changed to a different value during flight. The radiances, fluxes, and cloud identifications at the top of the atmosphere will make up the CERES first-level data. The American Aerospace contractor TRW is responsible for the design, manufacturing, and testing of the CERES instruments under NASA contract. The ERBE scanning instrument package is the basis for the CERES instrument design and calibration protocols. The CERES Science Team is developing mathematical models which will produce filtered radiances from the output signals at satellite altitudes, invert the radiances into fluxes at the top of the atmosphere, and guide the data processing

algorithms and ground/flight calibration interpretations. Each CERES instrument package will contain a shortwave (0.3 to 5 μm), a total (0.3 to 200 μm), and a water-vapor window (8 to 12 μm) thermistor bolometer sensor unit [13].

1.4 Goals and Motivations

The Thermal Radiation Group (TRG) at Virginia Polytechnic Institute and State University (VPI&SU) has been developing numerical models for analyzing instruments that measure the Earth radiation budget since the early 1970's. These studies evolved from the theoretical studies of the radiative characteristics of spherical cavities by Fanney [14], Rasnic [15], and Passwaters [16]. Eskin [17] was the first to use the Monte-Carlo ray-trace method to perform a radiative analysis of the ERBE nonscanning radiometers. Gardiner [18] and Tira [19, 20] also analyzed the nonscanning radiometers. An optical analysis of the ERBE scanning radiometer was completed by Meekins [21]. Haeffelin [22] completed a dynamic electrothermal model of the CERES instrument which can predict the output voltage of the electronic circuit for a given substrate temperature underneath the detector. This output voltage is the dynamic electrothermal response of the detector to incident radiation.

In order to design a radiometer that can measure the components of the Earth's radiation budget effectively and efficiently, we must understand, to the best of our ability, the behavior of the instrument under the given operating conditions. Since it is very difficult to determine the realistic behavior of the instrument, we can investigate its behavior for extreme cases. It can then be argued that if drastic changes do not occur in an extreme case, then these drastic changes will not occur in a realistic case. The extreme cases studied were:

1) steady-state space look,

2) steady-state Earth scene,

and 3) a simulated scan in which the instrument changes scenes from a steady-state space look to a steady-state Earth scene.

The steady-state space look temperature distribution provides the greatest temperature change which can occur within the instrument. A transient analysis based on the space look of the instrument will allow determination of the pseudo time constants. These pseudo time constants are the largest that the instrument can attain and can be used to simulate a scan from a steady-state space look to a steady-state Earth scene. The simulated scan will reveal the lowest temperature changes that will occur during a space to Earth scan. When the temperature distribution is known, the noise power contribution to

the detector from the interior surfaces of the instrument can be determined as a function of time. This power will characterize the amount of undesired thermal radiation incident to the detector at any instant during a real scan.

The Finite Element Method (FEM) is used by the author to obtain the temperature distribution for the appropriate boundary conditions. The finite element model of the CERES instrument in the current effort has been generated using commercial software packages: PATRAN and ABAQUS. PATRAN allows one to create a finite element mesh, define material and element properties, and specify the boundary conditions. ABAQUS then performs the analysis and generates an output.

The boundary conditions include a knowledge of the net radiative fluxes on the interior surfaces of the instrument. These have been determined by Bongiovi [12]. He subdivided the instrument geometry into 746 surface elements and developed three models to obtain the distribution factors for each surface element via the Monte-Carlo ray-trace method. The distribution factor is the fraction of energy absorbed by one surface which has been emitted from another surface including direct radiation and all possible reflections (specular and diffuse) [23]. The first of Bongiovi's [12] models calculates the distribution factors between all the surfaces. These are a measure of the actual input into the thermal conduction analysis at the surfaces of the instrument. The rays are initially traced from the active detector element. The number of rays traced from every other surface is then scaled by the product of the number of rays emitted by the active detector element and the

area ratio of the particular surface to that of the active detector element $\left(N_{surface} = N_{detector} \frac{A_{surface}}{A_{detector}}\right)$. In order to compute the distribution factors between all of the surfaces within the instrument it is appropriate to compute the distribution factor from the smaller surfaces to the larger ones. Then, the distribution factors from the larger surfaces to the smaller ones can be determined via reciprocity

$$\varepsilon_i A_i D_{ij} = \varepsilon_j A_j D_{ji} , \qquad (1.1)$$

where

i is the emitting surface,

j is the absorbing surface,

ε is the emissivity,

A is the area,

and D is the distribution factor.

The second of Bongiovi's [12] models calculates the radiation which affects the active detector element. The distribution factors from the active detector element to the rest of the surfaces are calculated instead of those between all the surfaces of the instrument. This requires that rays be emitted only from the active detector element. One can

determine from these distribution factors the power absorbed by the active detector element. This power is the thermal noise caused by emission from the remaining of the instrument's interior surfaces. The third model performs an optical analysis. The energy bundles are emitted from an imaginary surface covering the aperture of the instrument. Emission may be collimated or diffuse, and wavelength-dependent characteristics of the filters and mirrors may be taken into account. Rather than the distribution factors, this model directly computes the percent of energy incident to the aperture from the external scene that is absorbed by each surface. The reader interested in more information on these models is referred to Bongiovi's Master of Science Thesis [12].

2.0 Radiometers

2.1 Infrared Detectors

The following discussion on infrared radiometers is based on a report by Astheimer [24].

According to Astheimer two types radiometer are manufactured today, those based on photon counting and those based on thermal effects. Photon detectors operate on the principle of absorption of an infrared radiation photon by a semiconductor electron whose energy level is then elevated into a conduction band. A signal cannot be produced by photons with lower energies than that of the band gap. Cooling the photon detectors is necessary in order to prevent any excess ambient temperature-induced conduction of

electrons. Thermal detectors operate on the principle of infrared radiation absorption by a temperature-sensitive element. The Golay detector is an exception because infrared radiation is sensed by a change in pressure of a gas. This pressure change is caused by a temperature change resulting from the absorbed infrared radiation.

The thermal infrared detectors used to be the most common because photon detectors appeared on the scene in only the late 1940's. Thermocouple detectors and wire-wound resistance thermistor bolometers are low-impedance thermal infrared devices producing minuscule signals which in most cases cannot be amplified with vacuum-tube technology. Thermocouple detectors were more common than the wire-wound resistance thermistor bolometers [24].

Thermistors are thermally dependent resistors developed at Bell Laboratories during World War II. They possess a high resistivity and can exploit the large, negative temperature coefficient of resistivity of semiconductors. Thermistor manufacturers use two formulations: no. 1 material, a mixture of nickel and manganese oxides, and no. 2 material, a mixture of nickel, cobalt, and manganese oxides. The thermistor detector elements used on CERES are built by Servo Inc. under subcontract to TRW. The ferrous oxide powders are mixed with an organic binder to form a thin creamy slurry film which is spread more or less uniformly on a glass plate and dried. The elements are cut from the resulting sheet into rectangular shapes and baked in an oven at the sintering temperature while attached to smooth ceramic plates. Gold electrodes are attached along opposite

sides to which lead wires are then bonded. The flakes are approximately 10 μm thick and the sensitive areas between electrodes can range anywhere from 0.05 × 0.05 mm to 5 × 5 mm.

Thermistor elements are commonly used for infrared detection. They are configured in various ways and must be thin so that both the heat capacity and the temperature change are minimized when radiation is absorbed. Stability of the sintered structure is very important in order to prevent the bias current from producing any excess noise which can obscure a reading of the resistance change. The lead attachments must also be current-noise free. The thermistor element, also referred to as a "flake", is then mounted onto a heat sink [24]. The flake is separated from the heat sink by a thermal impedance, usually a layer of Kapton, allowing the temperature of the flake to increase when it is heated. Without this thermal impedance layer, the flake would remain at the heat sink temperature [25].

The sensing area is coated with a black absorber layer to improve the absorptivity of infrared radiation. The black coating has the detrimental effect of increasing the heat capacity and thus the time constant of the flake. At wavelengths below 2 μm and above 15 μm, the absorption is greater than 90 percent. At wavelengths ranging from 3 to 14 μm, the black coating will more than double the response.

Infrared radiation impinging upon the flake is absorbed, thereby slightly increasing the temperature of the flake and envoking a small resistance decrease of the thermistor. This

resistance change produces an electrical current when a bias voltage is placed across the thermistor. The current is then measured with a two-active-arm bridge circuit comprised of two identical flakes. The CERES bridge circuit is shown in figure 4. One flake receives the radiation to be sensed and is called the active flake, and the other is isolated from radiative inputs and is called the compensator. The bias voltages applied across the two thermistor flakes are equal, allowing maintenance of the potential at the junction point near zero, independent of ambient temperature variations. As a result, the signal output is less dependent upon the heat sink temperature because the same average resistance is maintained by the active and compensating flakes and no deflection of the bridge occurs. When radiation is absorbed by the active flake, the resulting temperature change between the active and compensating flakes causes the bridge to deflect and produce the signal from which the corresponding heat flux may be found [24].

2.2 CERES Instrument Description and Operation

The following discussion concerning the description of the CERES instrument is based on reference [12]. The CERES instrument design is similar to the ERBE design, but with improved features to meet higher standards in performance. The CERES instrument is shown in figure 5. Both CERES and ERBE are three-channel instrument packages. In both experiments one channel is sensitive to reflected shortwave energy in the 0.3 to 5 μm

range and to total radiation in the broadband spectral region from 0.3 to about 50 μm. The ERBE longwave channel responds in the range between approximately 3.5 to 50 μm, while in CERES this channel will be replaced by a channel capable of surface temperature observations in the atmospheric "window" between 8 and 12 μm. This particular configuration will improve measurements of the surface longwave flux, which will provide a measure of the "greenhouse" effect [11]. The shortwave detector has a Dynasil fused-quartz filter while the atmospheric window detector has one filter made of zinc sulfide and another one made of cadmium telluride [27].

The main component of the CERES instrument is the Cassegrain telescope. This telescope consists of a hyperboloidal secondary mirror and a paraboloidal primary mirror. Incoming on-axis radiation is first intercepted by the primary mirror, reflected off its surface toward the secondary mirror. It is then reflected from the secondary mirror and focused onto a thin-film thermistor bolometer placed near the focal point of the system. Radiation entering at an angle which is greater than a narrow allowable off-axis angle is rejected by the instrument. The Cassegrain telescope is illustrated in figure 6 and an exploded view of the instrument is shown in figure 7.

The baffle of the instrument is made out of an aluminum alloy and is cylindrical. Its interior contains five spaced thin rings whose inner radii decrease with increasing distance from the aperture. The surfaces of the rings facing the aperture are highly polished in order to reject any incoming off-axis radiation beyond the allowable angle, while the

surfaces facing the active flake are coated with Chemglaze™ black paint. The absorptivity of this coating is approximately 0.9. The baffle also contains two conical sections at its base which are highly polished to reflect undesired incident radiation back towards the aperture.

To further prevent undesired radiation from contaminating the instrument, a reflector cap is placed below the baffle. The reflector cap contains a series of conical sections consisting of surfaces facing the aperture and the active flake. Surfaces facing the aperture are highly polished and act as reflectors of stray radiation while surfaces facing the active flake act as absorbers.

The shortwave and longwave channels have a filter below the reflector cap. The longwave filter is composed of zinc sulfide and the shortwave filter is composed of Suprasil-W2 silica glass. These filters reject incoming radiation in the unwanted wavelength ranges.

The secondary mirror is located below the reflector cap. It is held in place by a cylindrical housing which is attached to three extensions, called "spider legs," placed at 120-deg intervals. The mirror is coated in order to protect it from degradation due to ultraviolet radiation.

The telescope housing contains the Cassegrain telescope. The secondary mirror is located at the top of the telescope and the primary mirror is located at the bottom. The housing has several V-grooves coated with Chemglaze™ containing glass microballoons.

This results in predominantly specular rather than diffuse reflection. This means that most radiation approaching the V-groove is either absorbed or is specularly reflected back onto an absorbing surface before escaping.

The primary mirror and its insert are located at the bottom of the telescope housing. The primary mirror insert rests in the primary mirror. The primary mirror is highly reflective and coated to prevent ultraviolet radiation from damaging it, while the primary insert is coated with copper black. Radiation passes through an opening at the inner diameter of the primary insert.

The field stop is located below the primary insert. Its main purpose is to limit the angle of incidence of the radiation entering the instrument that reaches the detector. The field stop is made out of copper and is painted black on the surface facing the baffle aperture to absorb any undesired radiation. A field stop retainer sits on top of the field stop. The retainer is an aluminum washer whose inner diameter is slightly larger than that of the primary insert to prevent any motion of the insert.

The field stop sits on an aluminum spacer. The second filter found in the shortwave and longwave channels sits inside the spacer since its outer diameter is smaller than the inner diameter of the spacer. This filter is made out of zinc sulfide in the longwave channel and Suprasil-W2 silica glass in the shortwave channel.

The detector, or active flake, is located directly below the aperture of the field stop. This component and the identical compensator are mounted on a heat sink and are composed of seven layers [12]. The active flake is shown in figure 8.

The finite element model of the CERES instrument is presented in chapter 3 followed by a discussion of the results in chapter 4.

3.0 The Finite Element Model of the CERES Instrument

3.1 Finite Element Model Formulation

The mathematical formulation of the CERES scanner transient conduction problem may be obtained by the procedure described in the previous chapter. The differential equation governing the temperature distribution is the heat conduction equation [29] given by

$$\frac{\partial}{\partial x}\left(k\frac{\partial T}{\partial x}\right)+\frac{\partial}{\partial y}\left(k\frac{\partial T}{\partial y}\right)+\frac{\partial}{\partial z}\left(k\frac{\partial T}{\partial z}\right)-\rho c\frac{\partial T}{\partial t}+S=0, \qquad (3.1)$$

where

x,y,z are the cartesian coordinates (mm),

T is temperature (K),

k is the thermal conductivity of the particular material (W mm^{-1} K^{-1}),

ρ is the density of material (kg mm^{-3}),

c is the specific heat of the material (kJ kg^{-1} K^{-1}),

t is the time (s),

and S is the volumetric heat source/sink (W mm^{-3}).

Due to the operating conditions of the instrument, some simplifying assumptions have been made to reduce eq. 3.1 to a simpler form. These initial assumptions are,

1) steady-state, $\frac{\partial T}{\partial t} = 0$,

2) no internal volumetric heat generation, S = 0,

and 3) constant properties.

The first assumption was made because the steady-state temperature distribution provides the knowledge of the extreme values of temperature that the instrument can attain. These extreme values of temperature are the lowest that will occur within the instrument. The steady-state temperature distribution was obtained for two cases:

1) the space look,

and 2) a typical earth scene.

Knowledge of both distributions is important in determining the temporal radiative *noise* contributions to the active flake from several key components. These include the spacer, the field stop, the primary insert, the telescope housing, the secondary mirror mount, and the reflector cap. These components were identified in the earlier discussion of figure 7. The total contribution from these components is called the *thermal noise*.

The instrument is intended to operate in a nominal temperature environment ranging from 273.15 to 311.15 K. Since this is a rather restricted temperature range, the assumption that the variation in the thermal properties is negligible. The second assumption is patently true, since no internal heat generation occurs within the instrument. Under these assumptions equation 3.1 reduces to

$$\frac{\partial^2 T}{\partial x^2} + \frac{\partial^2 T}{\partial y^2} + \frac{\partial^2 T}{\partial z^2} = 0. \qquad (3.2)$$

3.2 Mesh Generation

When a differential equation is defined on a complex geometry (domain), it is almost impossible to obtain an analytical solution. The finite element method allows for subdivision of a complex domain into subdomains, defined by a set of node points, called *elements*. This process is also known as *discretization*. These elements have simple geometries and are much easier to analyze then the original domain. However, an error occurs when subdividing a given domain into elements because this subdivision is an

approximation to the original domain. The finer the mesh, the smaller the discretization error.

When discretizing a complex domain, it is important to keep track of the locations and numerical order of all the nodes. It is also important to know the neighboring elements when performing an analysis on a particular element and the elements surrounding a particular node. This knowledge is called *connectivity*. The connectivity must be defined in such a way that a node belonging to some element must correspond to a node belonging to some neighboring element [30].

Every element in the mesh has its own orientation and characteristic aspect ratio. An element to which all other elements are similar is called a *master element*. In this particular problem there are two master elements: the hex-shaped and the wedge-shaped element. These elements are illustrated in figure 9.

The linear elements have been chosen because they retain the geometrical shape of the instrument and the node bookkeeping is not too cumbersome. Linear elements are those in which the nodes are located only at their corners. The problem could have been modeled with quadratic elements but lack of memory and limited CPU time are potential problems that could arise if this path is chosen. Quadratic elements are those in which the nodes are located at the corners of the element and halfway between the sides containing two corner nodes. The finite element mesh of the CERES instrument is shown in figure 10. A software package combining PATRAN and ABAQUS [31-33] was used to generate the finite element model for the CERES scanner. First, the geometry of the

instrument was created by defining the appropriate grids, lines, patches (surfaces), and hyperpatches (volumes) of every component. This work required about three months to complete. First, all component dimensions had to be converted from inches to millimeters. Next, the finite element mesh for each component had to be developed based on its position with respect to other components. Finally, the geometry was created in PATRAN.

3.3 Model of the Boundary Conditions

The boundary conditions in the interior of the instrument were obtained from a full radiative Monte-Carlo analysis of the instrument [12]. In the full radiative model, each component is subdivided into large surfaces, and the large surfaces are then subdivided into smaller surfaces. A total of 81 large surfaces and 746 small surfaces comprise the model of the CERES scanner in reference 12. The surface names and their corresponding large and small surface numbers are given in Table 1. The small surfaces corresponding to the baffle were not included in the finite element model because the baffle is not conductively coupled to the rest of the instrument. However, the radiative contributions from the baffle surfaces have been included in the calculations of the net radiative heat fluxes on the remaining surfaces. Large surfaces 38 to 71 correspond to the baffle. The net heat flux on a given small surface j was determined by [23]

$$Q_{net,j} = Q_{out,j} - Q_{in,j}, \tag{3.3}$$

where

$$Q_{in,j} = \sum_i A_i \varepsilon_i \sigma T_i^4 D_{ij}, \tag{3.4}$$

$$Q_{out,j} = A_j \varepsilon_j \sigma T_j^4, \tag{3.5}$$

and $$Q_{net,j} = q_j A_j. \tag{3.6}$$

Substituting equations 3.4 through 3.6 into equation 3.3 and dividing both sides by A_j gives

$$q_j = \frac{1}{A_j}\left(\sigma A_j \varepsilon_j T_j^4 - \sum_i \sigma D_{ij} A_i \varepsilon_i T_i^4\right), \tag{3.7}$$

where

q_j is the net radiative heat flux from surface j (W mm^{-2}),

D_{ij} is the distribution factor from i to j,

A_i is the area of surface i (mm^2),

ε_i is the emissivity of surface i,

T_i is the temperature of surface i (K),

A_j is the area of surface j (mm^2),

ε_j is the emissivity of surface j,

T_j is the temperature of surface j (K),

and σ is the Stefan-Boltzman constant, (5.67×10^{-14} W mm^{-2} K^{-4}).

Factoring out σ, equation 3.7 becomes

$$q_j = \frac{\sigma}{A_j}\left(A_j\varepsilon_j T_j^4 - \sum_i D_{ij}A_i\varepsilon_i T_i^4\right). \qquad (3.8)$$

In order to calculate the heat flux q_j, the temperature of every interior surface was initially assumed to be at 311.15 K. An iterative procedure would then be adapted in which the calculated temperature distribution would then be used to recalculate new heat flux boundary conditions at the interior surfaces. These new heat fluxes would then be re-applied on the interior surfaces and a new temperature distribution would once again be calculated. This iterative procedure would continue until the change in the heat flux boundary condition was negligible. Since T_i is equal to T_j in this case, the fourth power of T may be factored out of equation 3.8 to yield

$$q_j = \frac{\sigma T^4}{A_j}\left(A_j\varepsilon_j - \sum_i D_{ij}A_i\varepsilon_i\right). \qquad (3.9)$$

Once the heat fluxes for all small surfaces have been calculated, the heat fluxes for each large surface can be calculated by taking the area-weighted average heat flux for the corresponding small surfaces. The conductivities of the materials are necessary because the radiative flux is set equal to Fourier's law $\left(-k\frac{\partial T}{\partial r}\right)$ at the boundaries. The material conductivities are given in Table 2 and the boundary conditions for both the space look and earth scene are given in Table 3. Negative values of heat flux indicate that the surface is warming up and positive values indicate that the surface is cooling down. Because some surfaces in the Monte-Carlo mesh do not match directly with the surfaces in

the finite element mesh, some approximations in distributing the heat fluxes had to be made. These are listed in Table 4. The elements generated in the Monte-Carlo mesh differ in shape, size, and quantity from the elements in the finite element mesh. The Monte-Carlo mesh consists of twelve similar elements for each interior surface of the instrument, while the quantity, size, and shape of the elements in the finite element mesh vary for different interior surfaces according to stacking of the instrument components. When the Monte-Carlo method is applied to a particular surface the connectivity of the mesh need not be defined in any particular manner; however, in the finite element method the connectivity of the mesh has to be defined in a specific way. Once the heat fluxes for all large surfaces of the Monte-Carlo mesh have been approximated, the corresponding large surface in the finite element mesh needs to be located in order to apply the correct heat flux to the correct surface.

The mounting tabs of the telescope housing of the instrument are thermally isolated from a support plate by a mica insulator. The support plate/insulator configuration is shown in figure 11. The support plate will undergo a nominal temperature variation in the range of 287.15 K to 297.15 K during the orbit of the satellite. This temperature boundary can be modeled by applying the appropriate temperature at the interface between the support plate and the insulator. It was not practical to construct the correct surface shape of the insulator because of finite element mesh limitations, which require that the surface shape of the insulator be the same as the surface shape of the tab. Since the thickness of the insulator was significantly less than any of its other dimensions,

conduction within the insulator is predominantly through its thickness. This allows the application of a resistance approach to calculate the equivalent thickness of the insulator to compensate for the incorrect area. The resistance is given by

$$R = \frac{L}{kA}. \tag{3.10}$$

Setting the resistance of the actual insulator equal to the resistance of the model insulator gives

$$\frac{L_{actual}}{kA_{actual}} = \frac{L_{model}}{kA_{model}}. \tag{3.11}$$

Solving for thickness of the model insulator gives

$$L_{model} = L_{actual} \frac{A_{model}}{A_{actual}}. \tag{3.12}$$

The CERES scanner has a heating element wrapped around the telescope housing slightly below the mounting tabs. This was modeled as a heat flux boundary condition in that region. The appropriate group of nodes, which approximately cover the heated region and the temperature sensor, was identified from a scale drawing. A heat flux boundary condition was applied to the elements containing nodes which correspond to the heater. This heat flux was determined iteratively by observing the average temperatures of the nodes chosen to represent the sensor. When this average was equal to 311.15 K for a given support-plate temperature, the heat flux was deemed correct. This method was used to obtain heater power as a function of support-plate temperature.

The remaining exterior surfaces of the instrument were modeled as insulated boundaries because their interaction with the rest of the environment is through radiation exchange with an environment at essentially the same temperature.

4.0 Results and Discussion

4.1 Results

The results obtained from the finite element model include:

1) the steady-state temperature distribution in the telescope structure during a space look for a support-plate temperature of 297.15 K,
2) demonstration of convergence of the finite element model as a function of the number of elements,
3) the heater power as a function of support-plate temperature,
4) the transient temperature distribution during a space look,

5) the transient temperature distribution as the instrument scans from a space look to an earth scene,

and 6) the transient change in total radiative power incident on the active flake for a complete scan from a space look to the earth scene.

Since the problem is linear, the extreme temperature boundary condition of 297.15 K at the insulator is set to 0 K. This produces a temperature range in the structure which is resolvable. If the real boundary temperature of 297.15 K had been used the variation from this temperature would have been too small to plot. In order to further increase the number of significant figures and to obtain an even better resolution of the temperature distribution, the temperatures at the interface of the insulator and the tabs were then applied as boundary conditions below the tabs in a second calculation. The artificial 0-K boundary was once again applied in this second calculation. The results reported are then interpreted as if 310.96 K has been subtracted from the temperatures of the remaining nodes. The temperature distribution T-310.96 is shown in figure 12. As discussed earlier, the temperature change that occurs within the instrument is greatest for this particular case. It can be seen that the variation in temperature within the instrument is negligible compared to the initial assumption of 311.15 K and as a result the variation in the heat flux boundary conditions is also negligible. This means that one iteration for the new temperature distribution is sufficient.

Figure 13 shows the heater power as a function of the number of elements. This graph is obtained by plotting the data from Table 5. The heater power was used as the

convergence criterion because, as discussed in the previous chapter, the heater power (heat flux boundary condition) required to maintain an average temperature of 311.15 at the nodes chosen to represent the control sensor should be independent of the number of elements in the model. A quadratic curve defined by

$$y = ax^2 + bx + c, \tag{4.1}$$

where was fit to the data in Table 5. The correlation coefficient is equal to unity, which means that equation 4.1 fits the data perfectly. All of the analysis reported here was performed on the 1251-element mesh. The error in heater power between the 1030-element mesh and the 1251-element mesh was 8 percent while the error between the 1251-element mesh and the 1444-element mesh was only 1.5 percent. The corresponding heater powers for the three meshes were, 1.08 mW (1030), 1.00 mW (1251), and 0.98 mW (1444). Because the difference in power between the 1251- and the 1444-element meshes is so small, the solution is considered to be converged.

Figure 14 shows the heater power as a function of the support-plate temperature. This graph is based on the data in Table 6. A straight line defined by

$$y = ax + b, \tag{4.2}$$

where has been fit to the data in Table 6. The correlation coefficient for this curve is 0.974, which means that 97.4 percent of the power varies linearly with decreasing support-plate temperature, as expected. According to a NASA source, 2.0 W have been budgeted for the heater on the CERES platform. The results reported here show that this will be more than sufficient.

The transient temperature distributions, for a space look with an initial temperature of 311.17 K, of the pertinent components are necessary in order to determine their time response. The time constants will be used to determine the thermal noise contribution of each component during transient operation. For successful instrument performance, it is desired to have a very small time constant for the active flake and a large time constant for the rest of the components of the instrument with respect to the time that it takes for the instrument to complete one scan. A single node is chosen to represent the average temperature of each component. The time response of the instrument was obtained by studying the transient solution for a space look. The time response of the components were interpreted in terms of pseudo time constants computed from the lumped capacitance approximation

$$T = T_i + \left[1 - e^{-t/\tau}\right]\left[T_f - T_i\right], \tag{4.3}$$

where

T is the temperature at a particular time (K),

T_i is the steady-state space-look temperature (K),

T_f is the steady-state earth-scene temperature (K),

t is the time (s),

and τ is the pseudo time constant.

A list of the steady-state space-look temperatures and the temperature differences between earth scene and the space look (T_f - T_i) for the components of interest is given in Table 7.

Equation 5.3 is a solution to a first-order differential equation, derived based on the lumped capacitance assumption

$$\rho Vc\frac{dT}{dt} = q_s^{"}A, \tag{4.4}$$

where

ρ is the mass density (kg mm^{-3}),

c is the specific heat (W kg^{-1} K^{-1}),

V is the volume (mm^3),

$q_s^{"}$ is the heat flux on the surface of the component (W mm^{-2}),

and A is the component surface area (mm^2).

Solving equation 4.3 for τ yields

$$\tau = \frac{t}{\ln\left[\frac{T_f - T_i}{T_f - T}\right]}. \tag{4.5}$$

ABAQUS can provide at most ten increments for a transient analysis. This means that a maximum of eleven data points may be obtained for a given transient problem. Recall that for this particular problem the solutions need to be incremented by 310.96 K because the boundary conditions were artificially biased by this amount.

The pseudo time constants were computed using the following procedure:

1) use equation 5.3 to compute the temperature at time τ (T_τ),

2) find two consecutive temperatures such that T_τ lies between them,

3) substitute the two temperatures and their corresponding times in equation 4.5 to obtain two pseudo time constants,

4) average the two pseudo time constants.

Equation 4.3 was plotted on those graphs to examine whether the lumped capacitance assumption can be justified. Equation 4.3 fits the data relatively well with the exception of the telescope housing. This means that the pseudo time constants are fairly reasonable representations of the physics and that the assumption of first-order behavior is reasonable for this particular problem. The assumption of first-order behavior can be further justified by the minute temperature variations within the instrument. The pseudo time constants of the relevant components are given in Table 8. The time constants for the substrate, spacer, field stop, and primary insert are relatively comparable to each other and large compared to those of the telescope housing, secondary mirror mount, and reflector cap. This difference in time response can be attributed to the fact that the energy must first flow through a large resistance (titanium spacer) before it reaches the active flake, spacer, field stop, and reflector cap. An *exterior node* and an *interior node* were chosen to calculate the time constants for the telescope housing. The exterior node corresponds to a node located at the outer edge of one of the cones, and the interior node corresponds to a node located at the vertex of two conical surfaces extending outward. The interior and exterior nodes are illustrated in figure 15. The telescope housing requires that two nodes be evaluated because the interior node is surrounded by more mass, meaning that its thermal capacity is greater than that of the exterior node. The pseudo time constant for

the interior node is 4.9 s, while that for the exterior node is 3.3 s. It can be seen from (figures 16 through 22) that the numerical solution follows an exponential decay. Overall, the time constants for all of the components other than the active flake are on the same order of magnitude as the time required for the instrument to complete a scan. Haeffelin [26], found that the time constant for the active flake is about 10 ms, which is very small compared to the scanning time of the instrument. This is exactly what is desired for successful instrument performance.

Once the pseudo time constants have been obtained, equation 4.3 can be used to represent the temperature variation in each component as the instrument scans from a steady-state space look to a steady-state Earth scene. These results indicate the extreme temperature distributions which the components of the instrument can attain during such a scan and are shown in (figures 23 through 29). It can be seen from these figures that the greatest temperature changes are on the order of mK.

Haeffelin [26] used equation 4.3 to compute the transient variation in thermal noise during two consecutive scan cycles. In computing the noise, Haeffelin assumed that the internal calibration temperature distribution is the same as that for the Earth scene. This result is shown in figure 30. The negatively sloped line segments corresponding to low noise powers represent variations in noise power during a space look, while the positively sloped line segments at higher power levels represent variations in noise power during an Earth scene viewing or during internal calibration. The nearly vertical line segments correspond to the almost instantaneous changes in power which occur when the

instrument scene changes. It can be seen from the graph that the variations in power during the space look are greater than those during Earth scene observation or observation of the internal calibration sources. This can be explained by the fact that the temperature difference between the instrument and its scene is the greatest when the instrument observes cold space.

5.0 Conclusions and Recommendations

5.1 Conclusions

It is concluded, based on the research reported in this thesis, that:

1. The finite element method has proven to be an effective tool for studying thermal noise sources in the CERES telescope structure.
2. The radiative boundary conditions contribute very little to the overall temperature distribution compared to the conduction due to the temperature difference between the heater and the support plate. It can be seen from Table 3 that the net power input due

to fluxes is very small compared to the heater power, most of which is dissipated by conduction to the mounting plate.

3. The thermal noise is sufficiently small to be considered negligible.

5.2 Recommendations

It is recommended that:

1. A dedicated computer code be written on first principles to model the transient behavior of the CERES telescope structure.
2. The Monte-Carlo mesh be made conformal to the finite element mesh, since the mesh connectivity is not an issue when applying the Monte-Carlo ray trace.
3. A software package be developed which can apply the Monte-Carlo ray trace to a finite element mesh.

Table 1. Names and numbers of large and small radiative surfaces.

Surface name	Large surface number	Small surface numbers
active flake sensor	30	1
flake substrate	37	2-25
spacer	36	26-37
bottom of field stop	29	38-49
top of field stop	28	50-73
extra telescope housing cones and telescope housing cylinder/rings	78, 79, 80, 81	182-193, 170-181, 74-85, 86-97
bottom cone of primary insert	34	98-109
inner cone of primary insert	27	110-121
top cone of primary insert	33	122-133
primary mirror	26	134-145
lip above primary mirror	32	146-157
telescope housing cylinder 2	25	158-169
telescope housing cone 2	34	194-205
telescope housing cone 1	23	206-217
telescope housing cylinder 1	22	218-229
upward facing lip of telescope housing	77	230-241

Table 1 (continued). Names and numbers of large and small radiative surfaces.

name of surface	large surface number	small surface number
secondary mirror mount (SMM) rim	31	242-283
conical perimeter of SMM	20	254-268
cylinder perimeter of SMM	19	269-280
surface of SM	21	281-292
SM housing inside cylinder	18	293-304
SM housing conic sections	76	305-316
perimeter of hub of SMM top ring	17	317-378
bottom ring	17	329-340
transition to spider legs	17	341-343
SMM hub	10	344-355
bottom of spider legs	14, 15, 16	356, 357, 358, 359, 360, 361
top of spider legs	11, 12, 13	362-365, 366-369, 370-373
reflector cap cylinder	9	374-385
lip between reflector cap and SMM	75	386-397
reflector cap cones	74, 73, 72, 1, 2, 3, 4, 5, 6, 7, 8	398-409, 410-421, 422-433, 434-445, 446-457, 458-469, 470-481, 482-493, 494-505, 506-517, 518-529

Table 2. Conductivities of materials used.

Material	Conductivity (W/mm K)
aluminum alloy	0.17700
copper	0.40100
titanium	0.02190
nickel	0.09070
glass	0.03800
mica	0.00016

Table 3. Space-look and earth-scene boundary conditions.

large surface number	space-look boundary condition (W/mm^2)	earth-scene boundary condition (W/mm^2)
30	2.03e-5	1.28e-5
37	-1.26e-7	-1.26e-7
36	-9.05e-8	-9.05e-8
29	-1.80e-7	-1.86e-7
28	6.55e-6	6.15e-6
80	3.85e-7	3.85e-7
81	-3.85e-8	-4.02e-8
34	1.09e-5	1.04e-5
27	5.86e-5	4.91e-5
33	6.09e-5	5.53e-5
26	0	0
32	3.91e-6	3.85e-6
25	2.15e-5	1.99e-5
79	-2.37e-5	-2.53e-5
78	-1.50e-5	-1.51e-5
24	-1.94e-5	-2.09e-5
23	-2.55e-5	-2.56e-5
22	-2.50e-5	-2.51e-5
77	3.53e-6	3.29e-6
31	2.83e-5	2.82e-5
20	1.76e-5	1.06e-5
19	-9.10e-6	8.82e-6

Table 3 (continued). Space-look and earth-scene boundary conditions.

large surface number	space look boundary condition (W/mm^2)	earth scene boundary condition (W/mm^2)
21	0	0
18	5.20e-5	5.17e-5
76	7.33e-5	6.60e-5
17	3.24e-5, 3.01e-5, 2.81e-5	2.64e-5, 2.63e-5, 2.26e-5
10	7.34e-6	4.69e-6
14	6.62e-5	6.34e-5
15	6.46e-5	6.21e-5
16	6.65e-5	6.37e-5
11	-1.33e-6	-1.86e-6
12	-1.70e-6	-2.20e-6
13	-1.71e-6	-2.24e-6
9	-1.53e-5	-1.56e-5
75	5.85e-6	5.55e-6
74	2.52e-5	2.49e-5
73	7.90e-6	-8.95e-6
72	1.19e-5	1.15e-5
1	-2.02e-6	-3.19e-6
2	-8.25e-6	-9.75e-6
3	-7.53e-6	-8.91e-6
4	-8.26e-6	-8.62e-6
5	4.72e-5	4.67e-5
6	1.23e-5	1.17e-5
7	2.78e-6	2.28e-6
8	5.37e-6	4.93e-6

Table 4. Redistribution of heat flux boundaries on the finite element model from the Monte-Carlo model.

Monte-Carlo large surface number(s)	finite element model boundary
36, 80	$q_{36} = q_{36} + q_{80}$
28, 29, 81	$q_{28,29} = q_{28} + q_{29} + q_{81}$
25, 32	$q_{25} = q_{25} + q_{32}$
17, 19, 20	$q_{17,19,20} = (q_{17} + q_{19} + q_{20})/3$
14, 15, 16	$q_{14,15,16} = (q_{14} + q_{15} + q_{16})/3$
11, 12, 13	$q_{11,12,13} = (q_{11} + q_{12} + q_{13})/3$

Table 5. Convergence of the heater power as a function of the number of elements.

number of elements	power (W)
1030	1.08×10^{-3}
1251	1.00×10^{-3}
1444	9.80×10^{-4}

Table 6. The support plate temperature and the corresponding heater power.

support plate temperature	power (W)
287.15	0.8686
289.65	0.7804
292.15	0.6921
294.65	0.6038
297.15	0.5155

Table 7. The steady-state space-look temperature and temperature difference results for nodes of the components contributing to thermal noise.

component name	steady-state space look temperature (K)	ΔT ($T_{earth\ scene}$ - $T_{space\ look}$) (mK)
active flake	311.1390	0.50
spacer	311.1389	0.50
field stop	311.1364	0.90
primary insert	311.1363	0.90
telescope housing		
exterior node	311.1262	0.20
interior node	311.1355	0.30
secondary mirror mount	311.0331	5.28
reflector cap	311.0913	0.30

Table 8. Pseudo time constants.

component name	time constant (s)
active flake	23.6
spacer	23.4
field stop	22.0
primary insert	21.9
telescope housing	
exterior node	3.3
interior node	4.9
secondary mirror mount	6.8
reflector cap	3.2

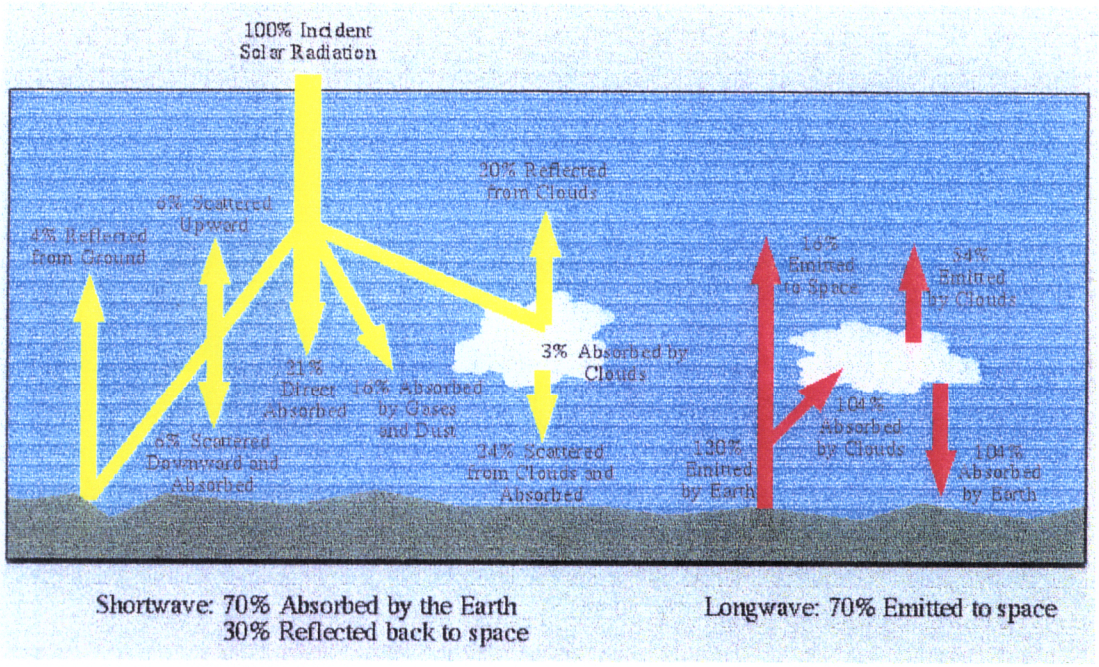

Fig. 1 The Earth Radiation Budget components [2].

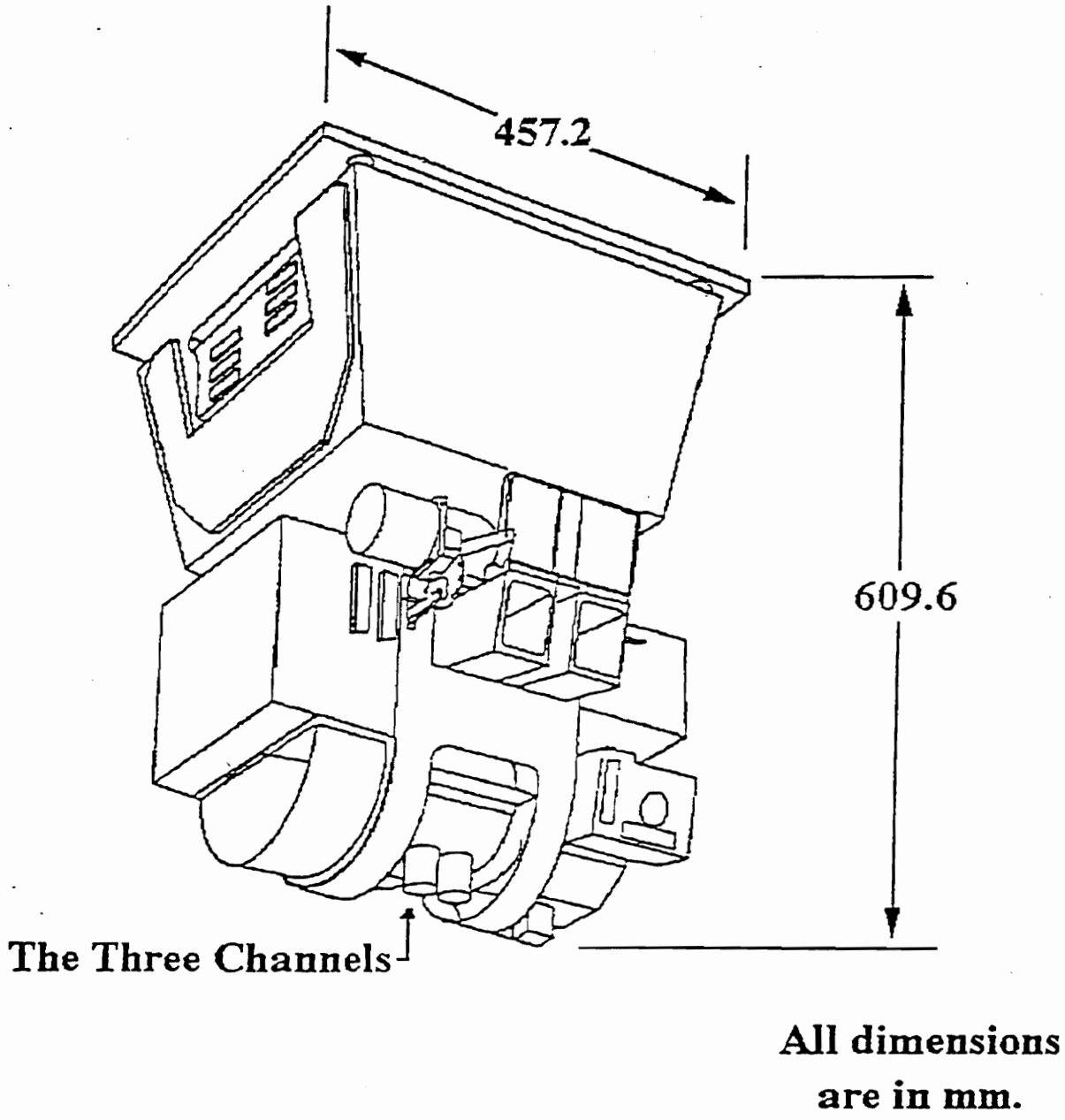

Fig. 2 The CERES scanning module [12].

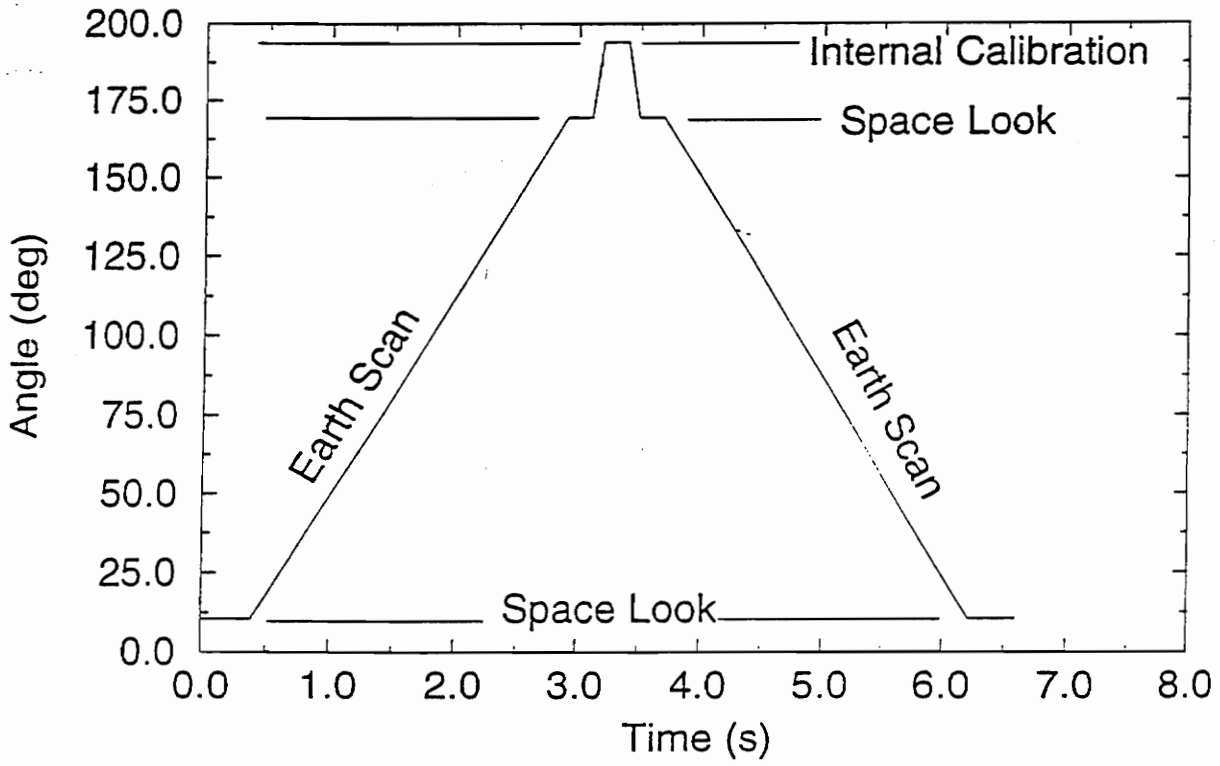

Fig. 3 The scan profile of the CERES instrument.

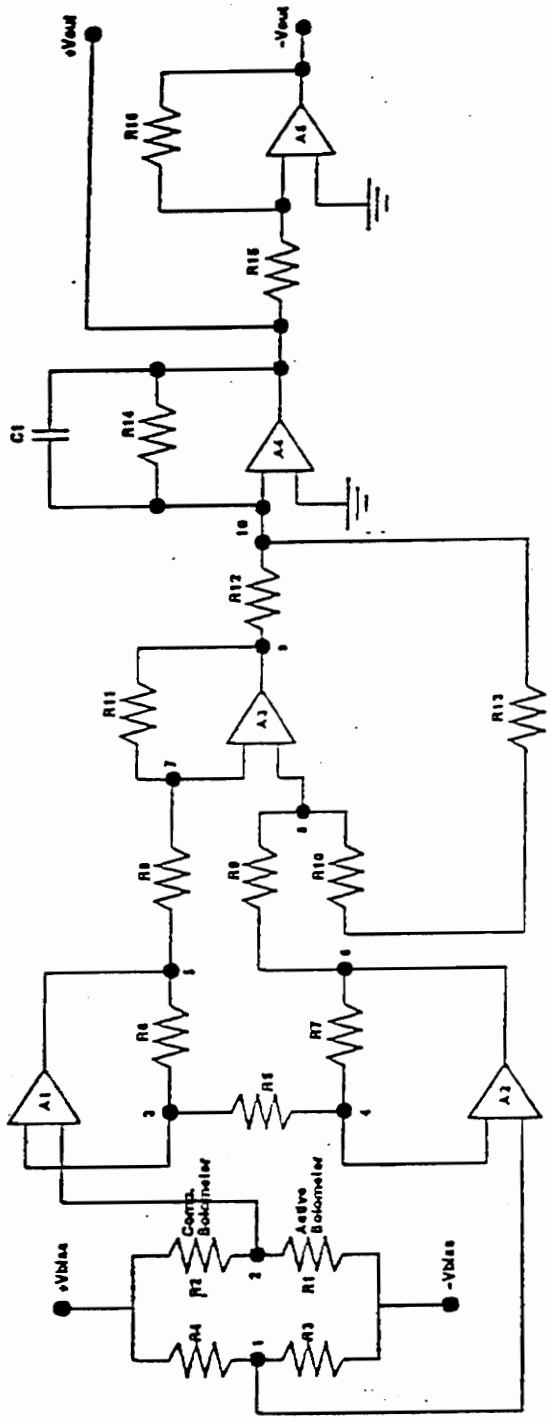

Fig. 4 The CERES Bridge Circuit [26].

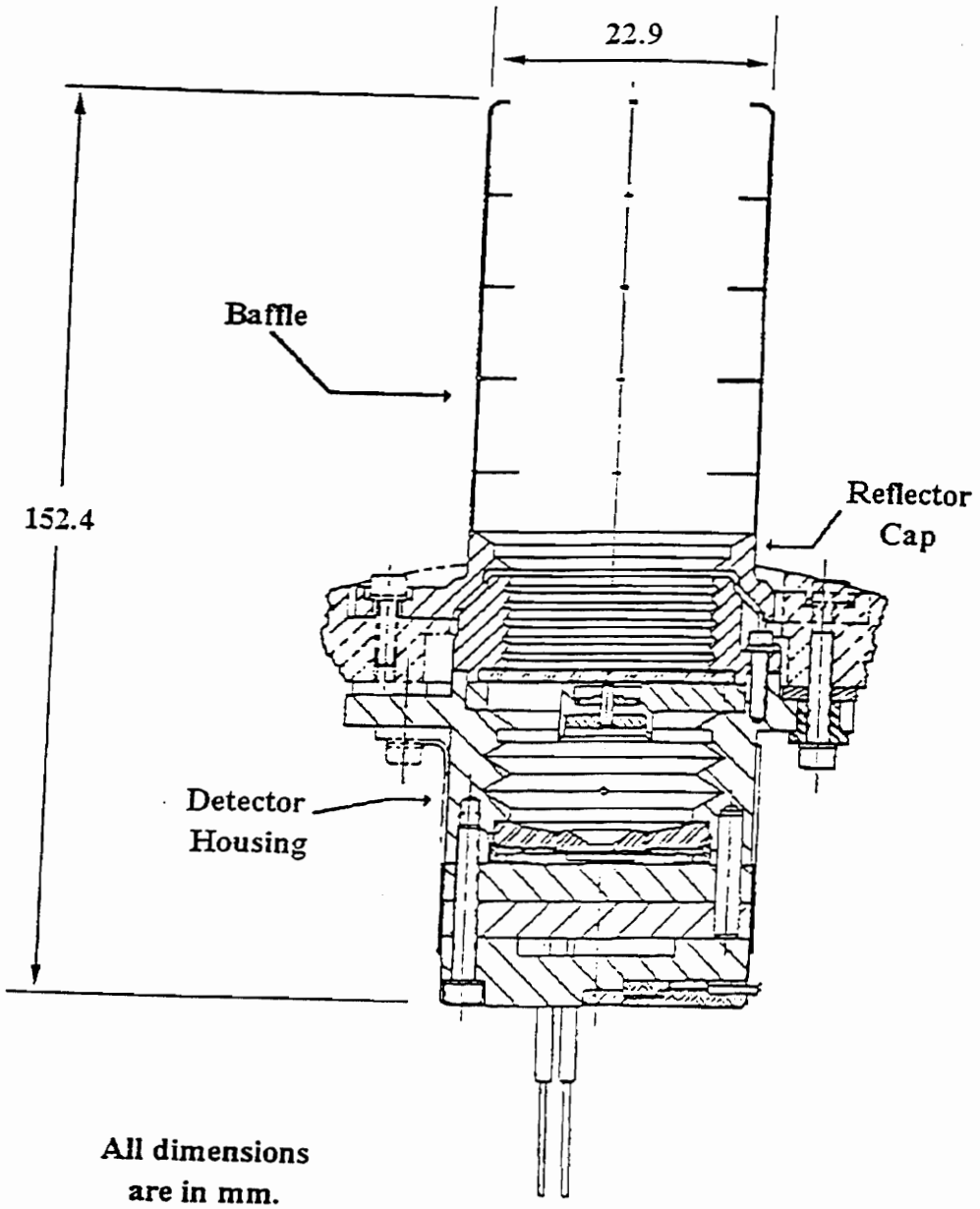

Fig. 5 The CERES scanning radiometer [12].

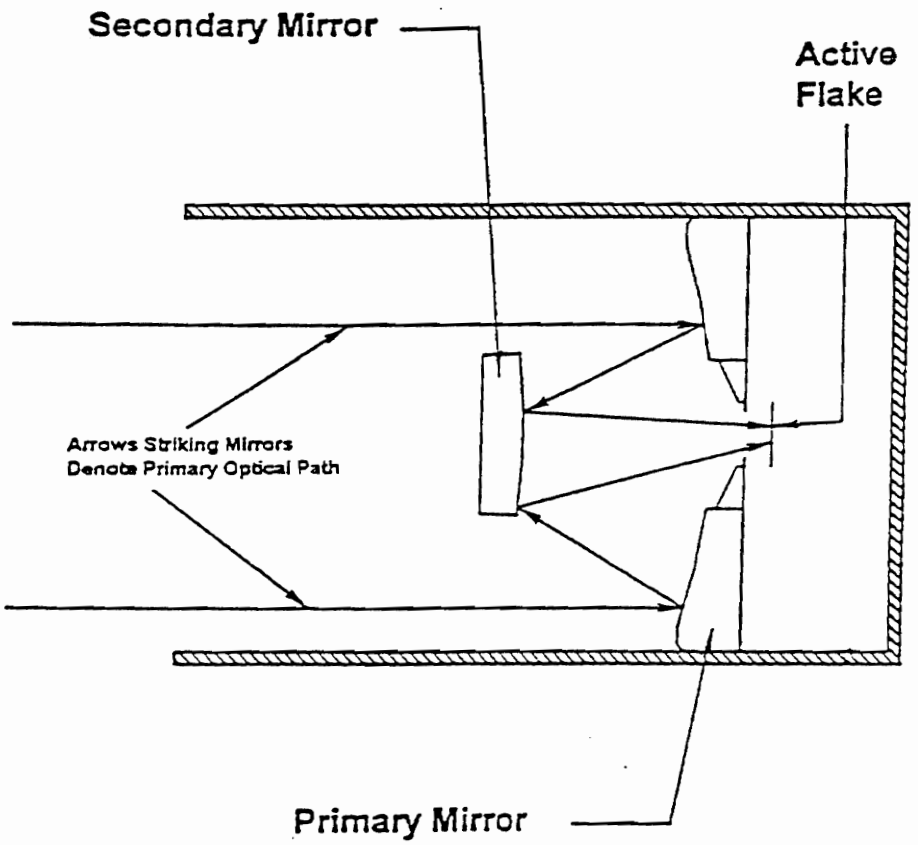

Fig. 6 The Cassegrain Telescope [12].

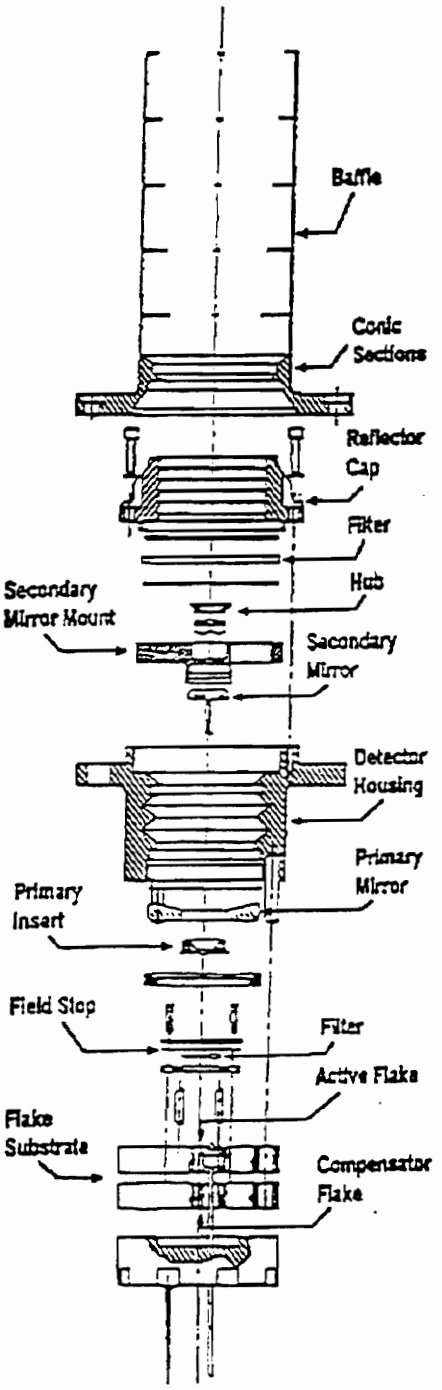

Fig. 7 The components of the CERES scanning radiometer [12].

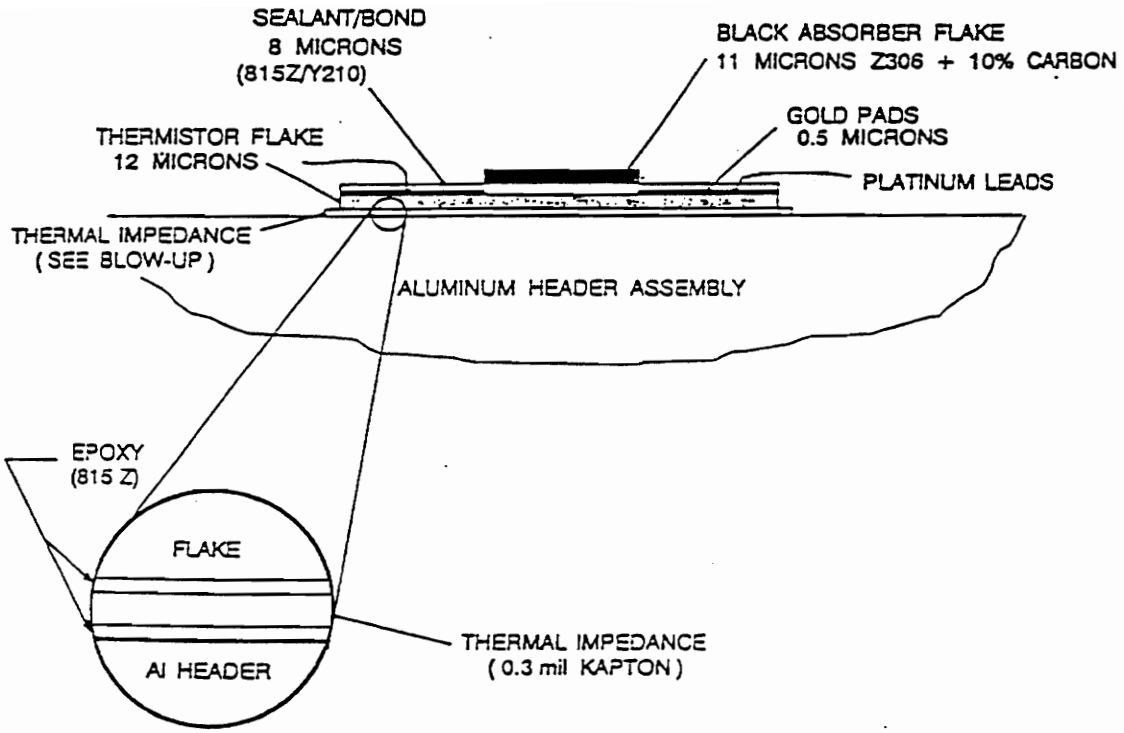

Fig. 8 The Thermistor Bolometer [28].

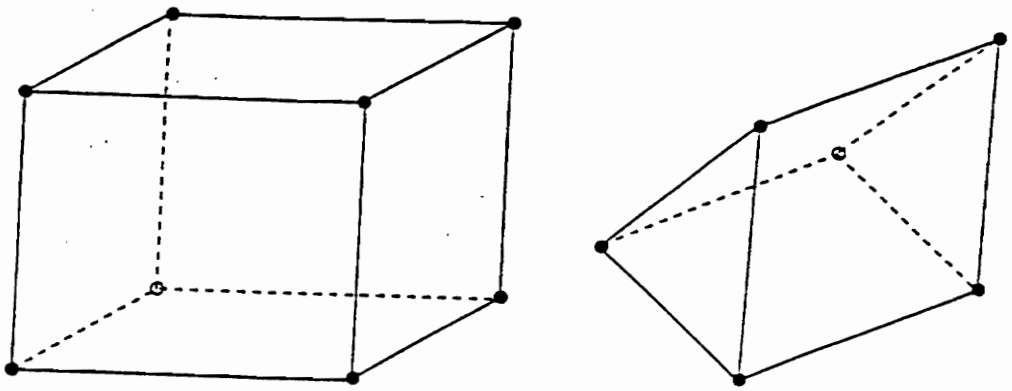

a) hex- shaped element

b) wedge-shaped element

Fig. 9 The master elements of the CERES finite element mesh.

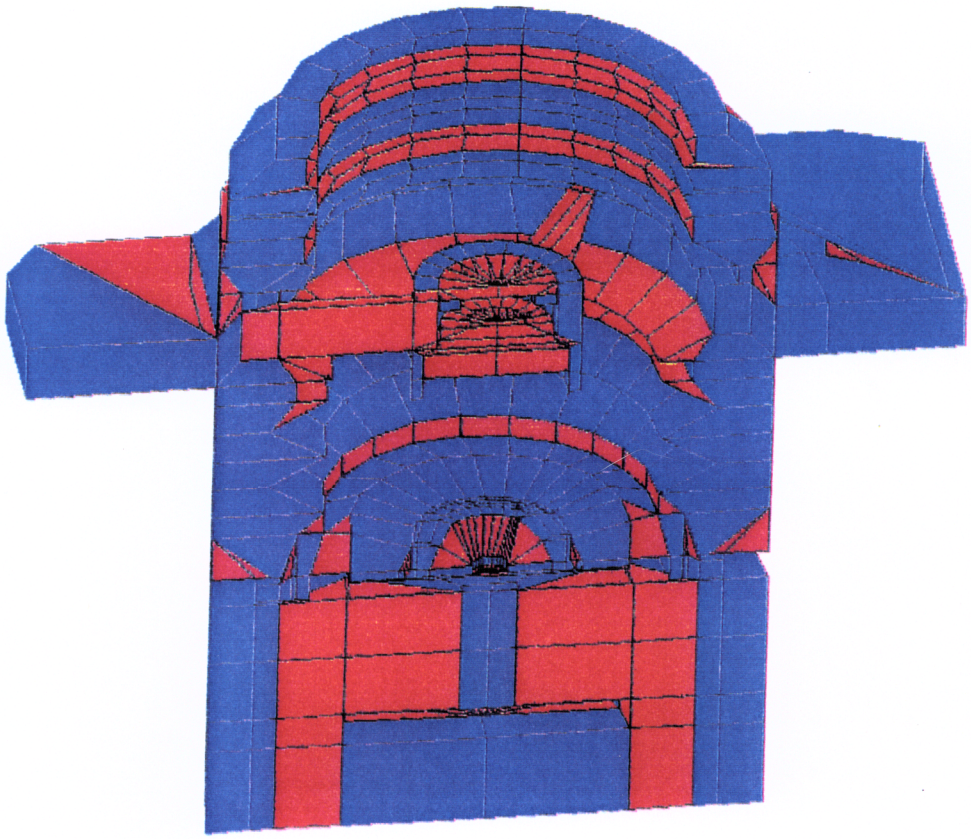

Fig. 10 The finite element mesh of the CERES scanning instrument (colors provided for readability).

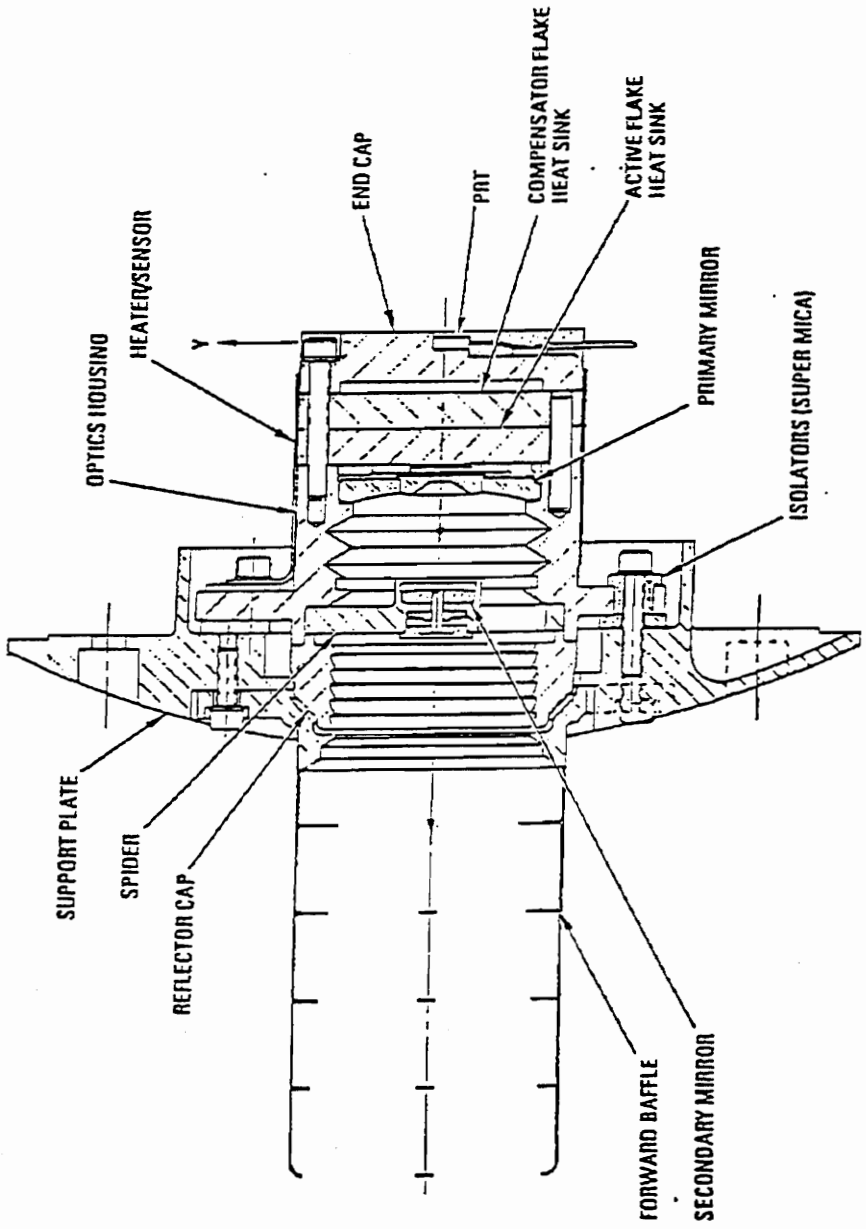

Fig. 11 The support plate/insulator configuration for the CERES instrument [28].

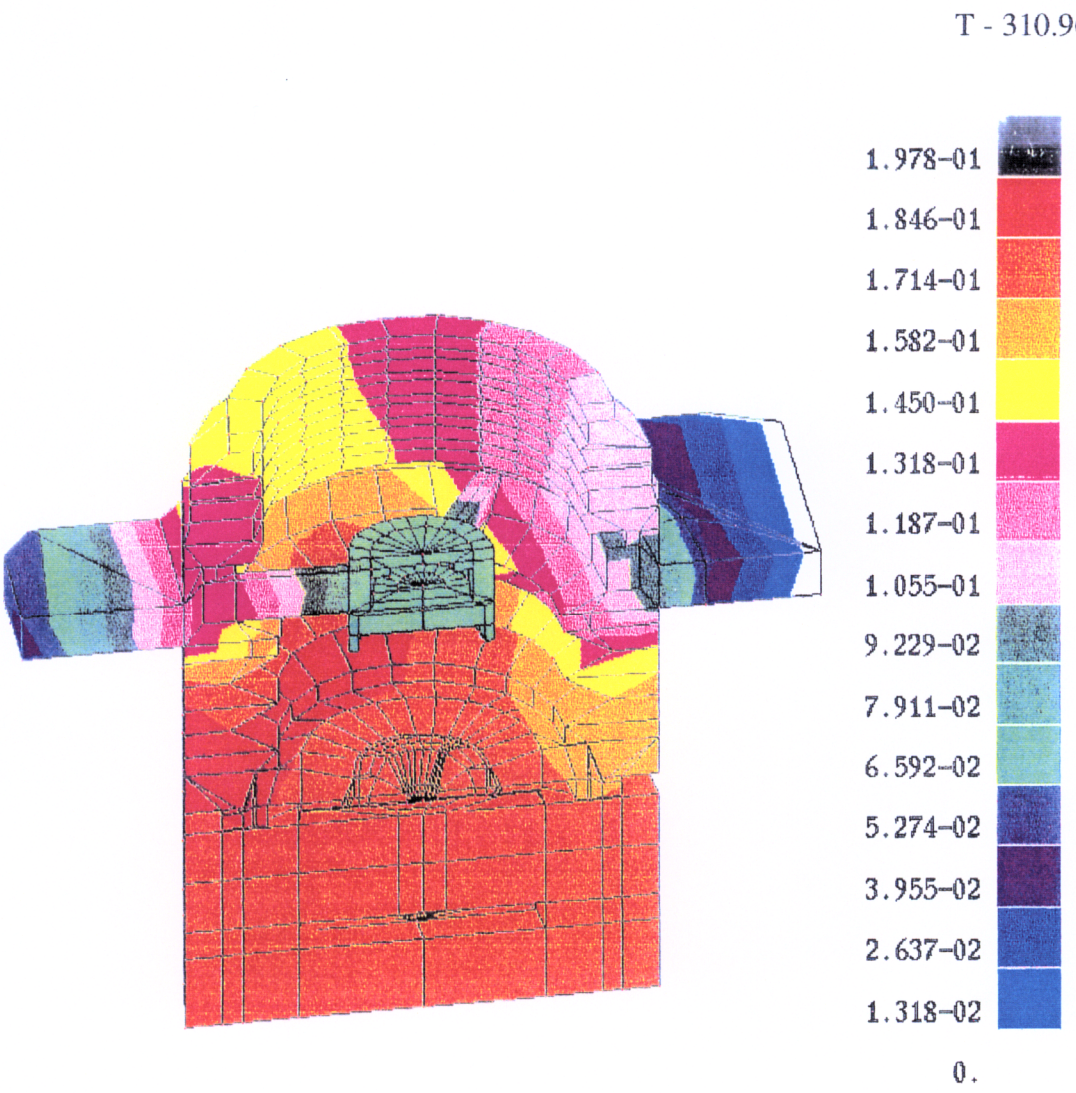

Fig. 12 The steady-state temperature distribution (T - 310.96) during a space look at a support plate temperature of 297.15K.

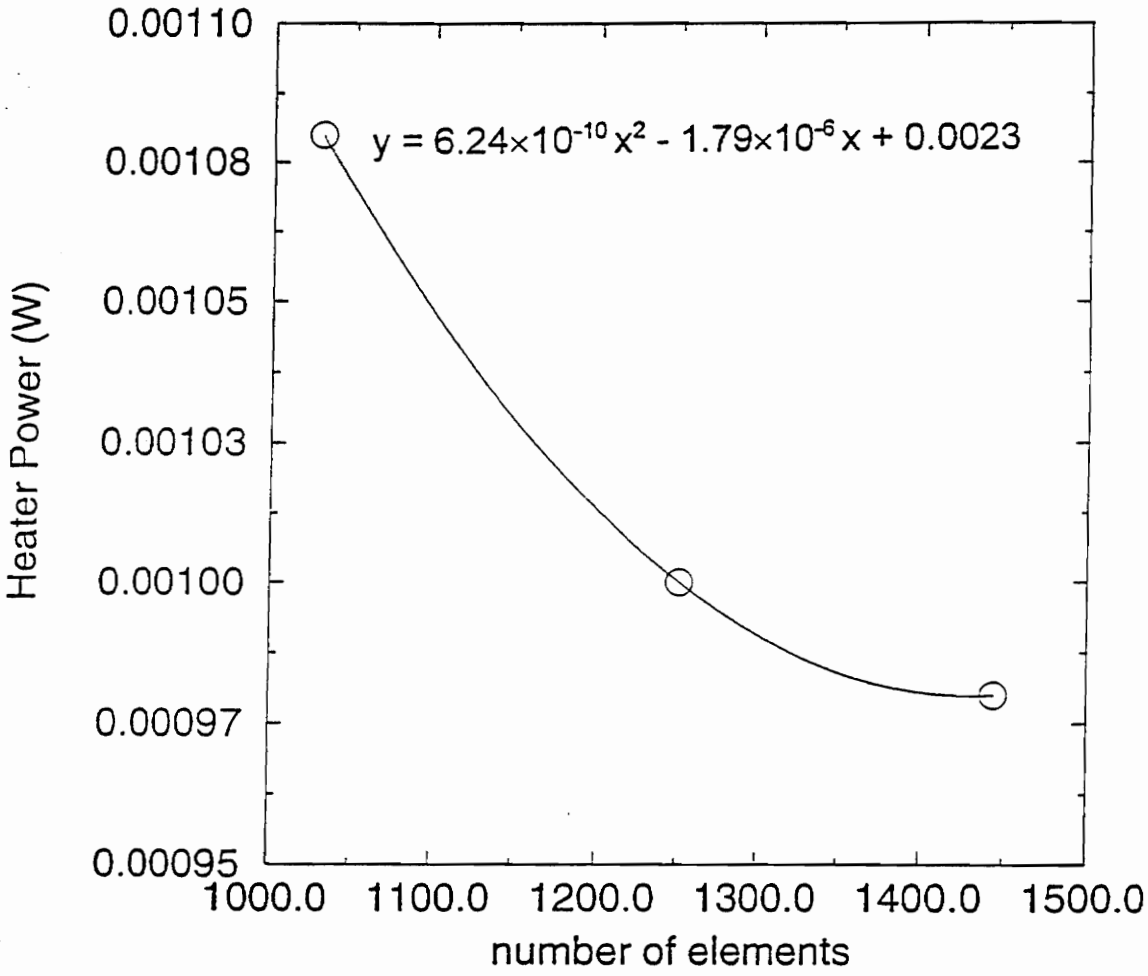

Fig. 13 Variation of heater power with the number of elements.

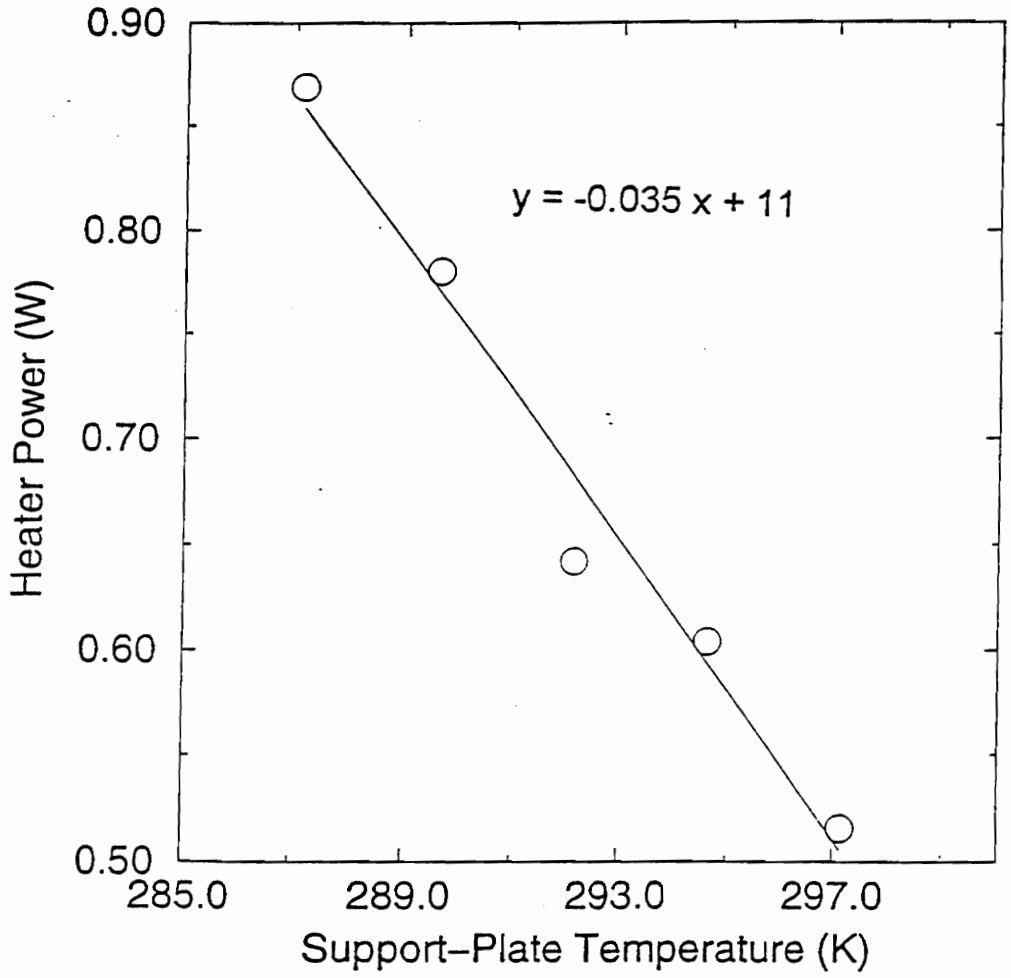

Fig. 14 Variation of heater power with support-plate temperature.

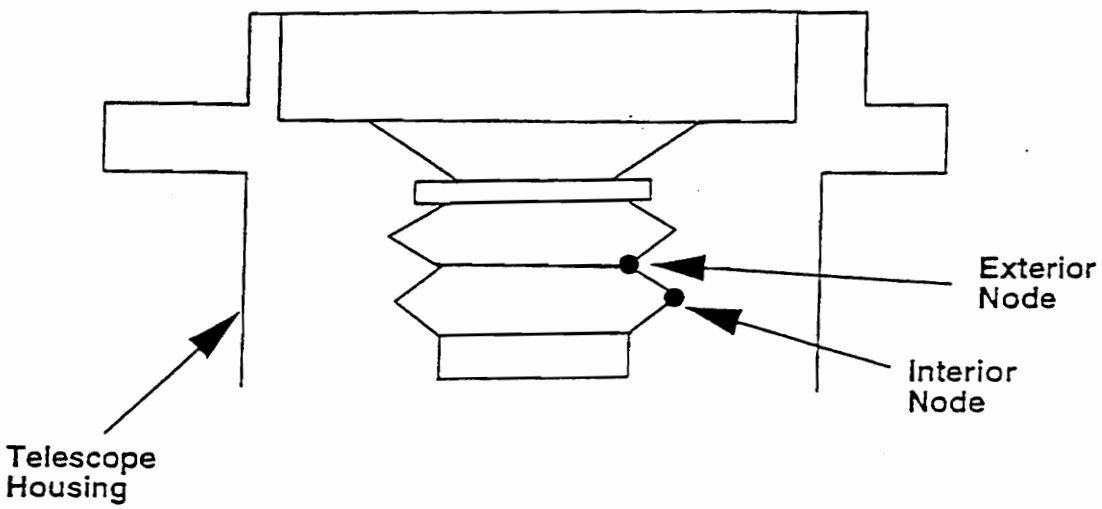

Fig. 15 An illustration of the interior and exterior nodes of the telescope housing.

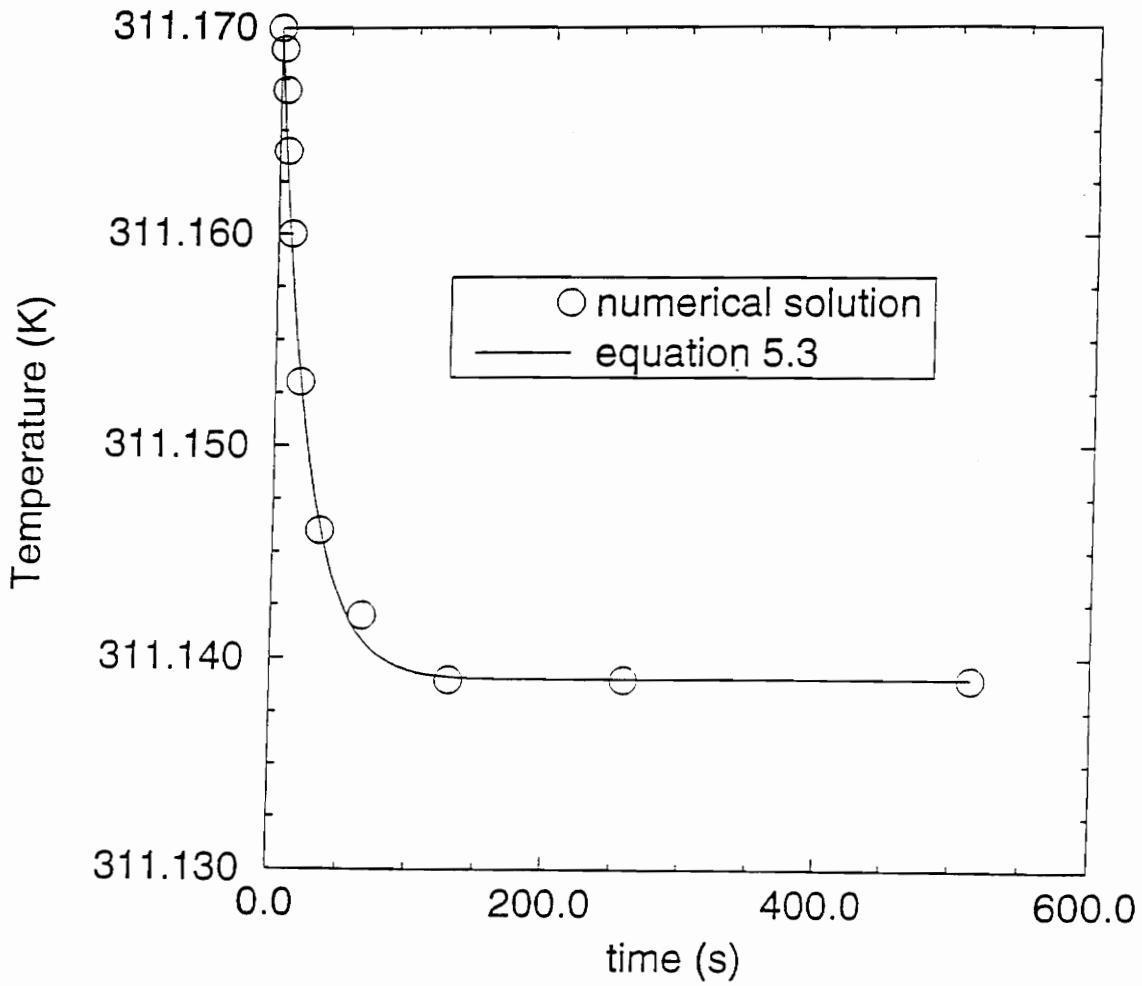

Fig. 16 Transient space-look temperature profile for a node under the active flake.

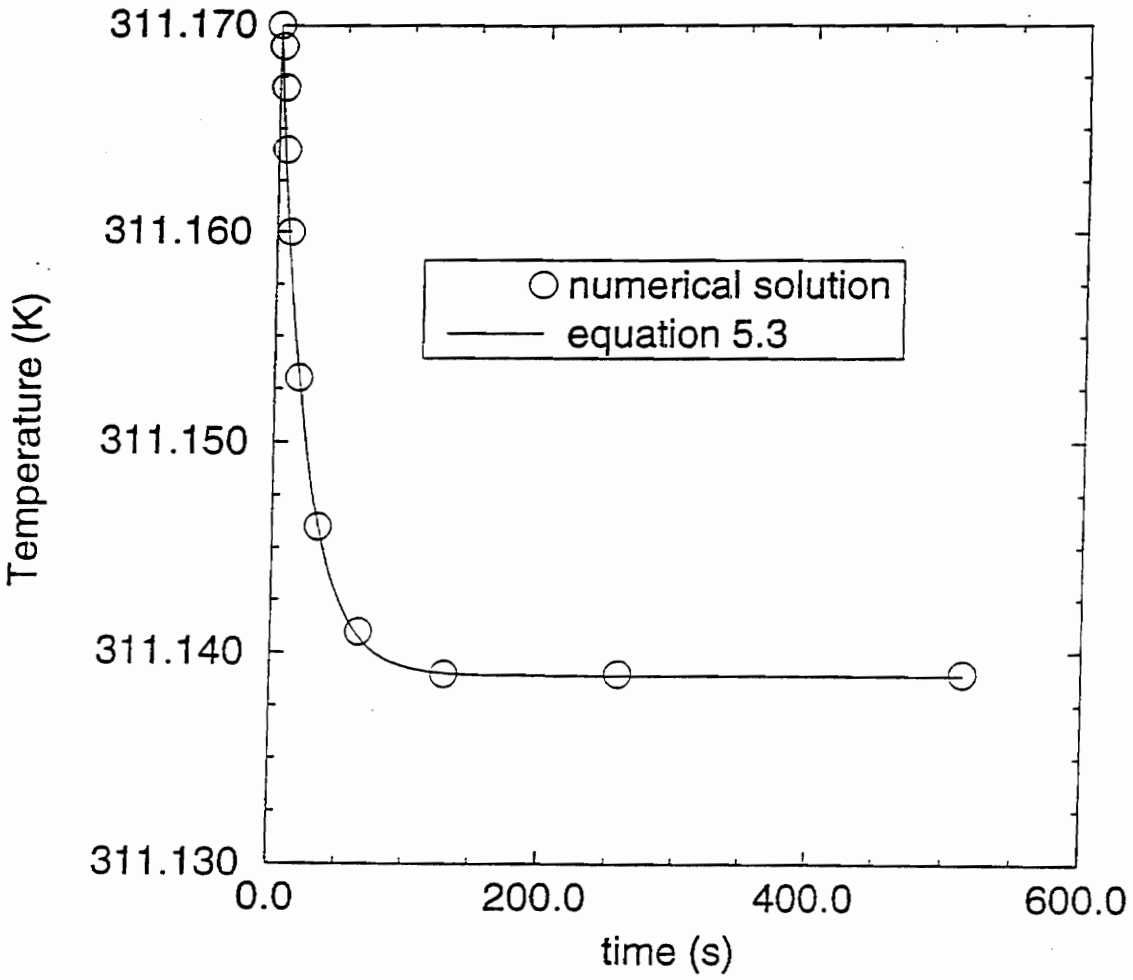

Fig. 17 Transient space-look temperature profile for a node on the spacer.

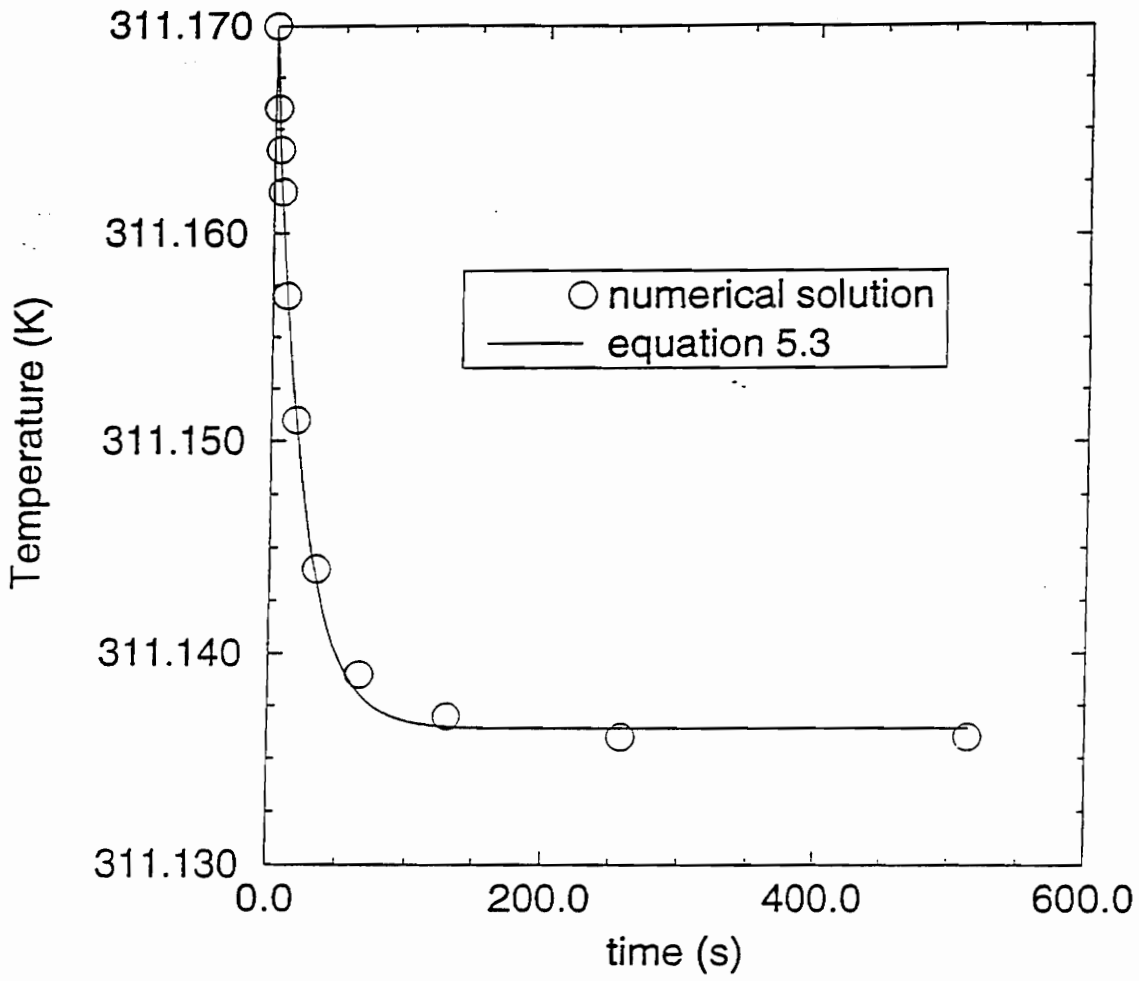

Fig. 18 Transient space-look temperature profile for a node on the field stop.

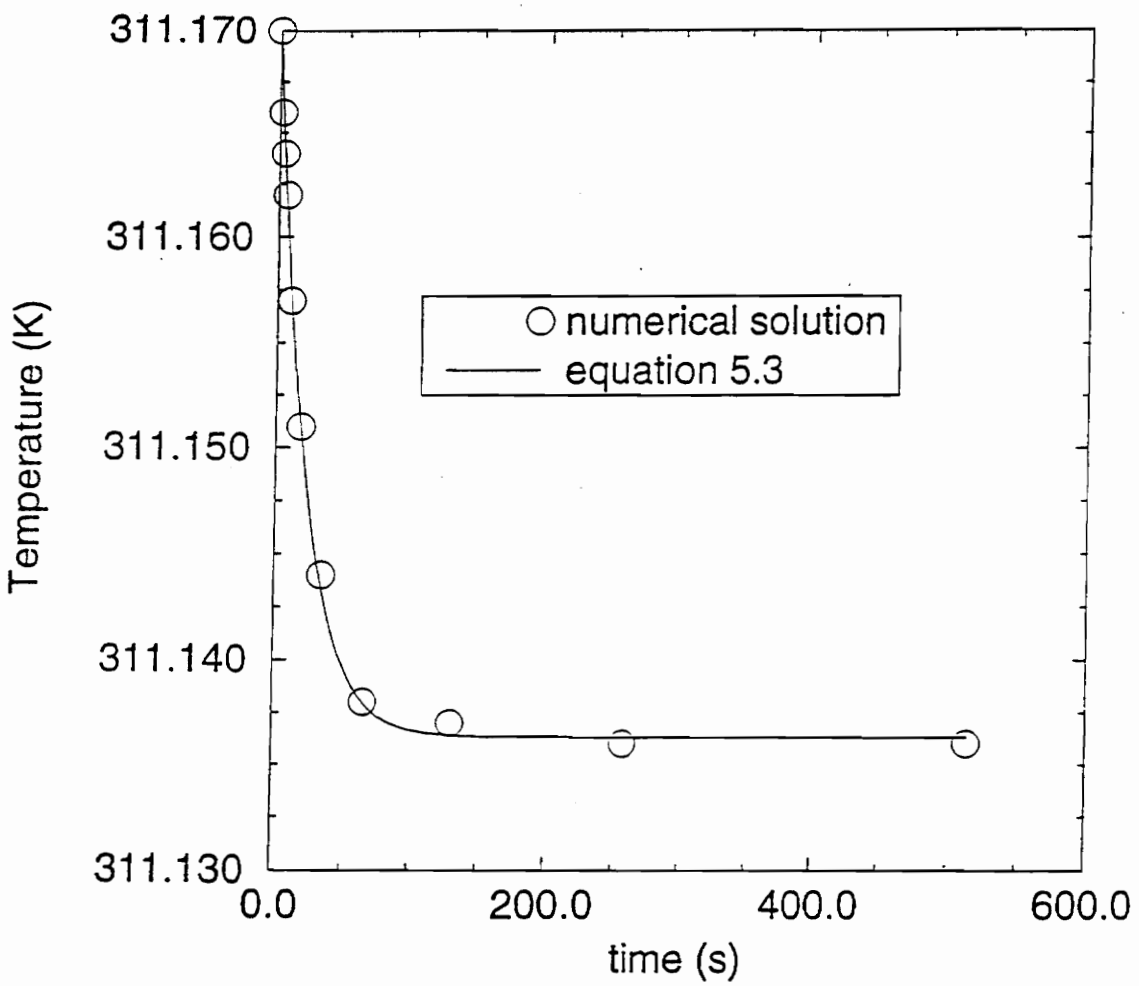

Fig. 19 Transient space-look temperature profile for a node on the primary insert.

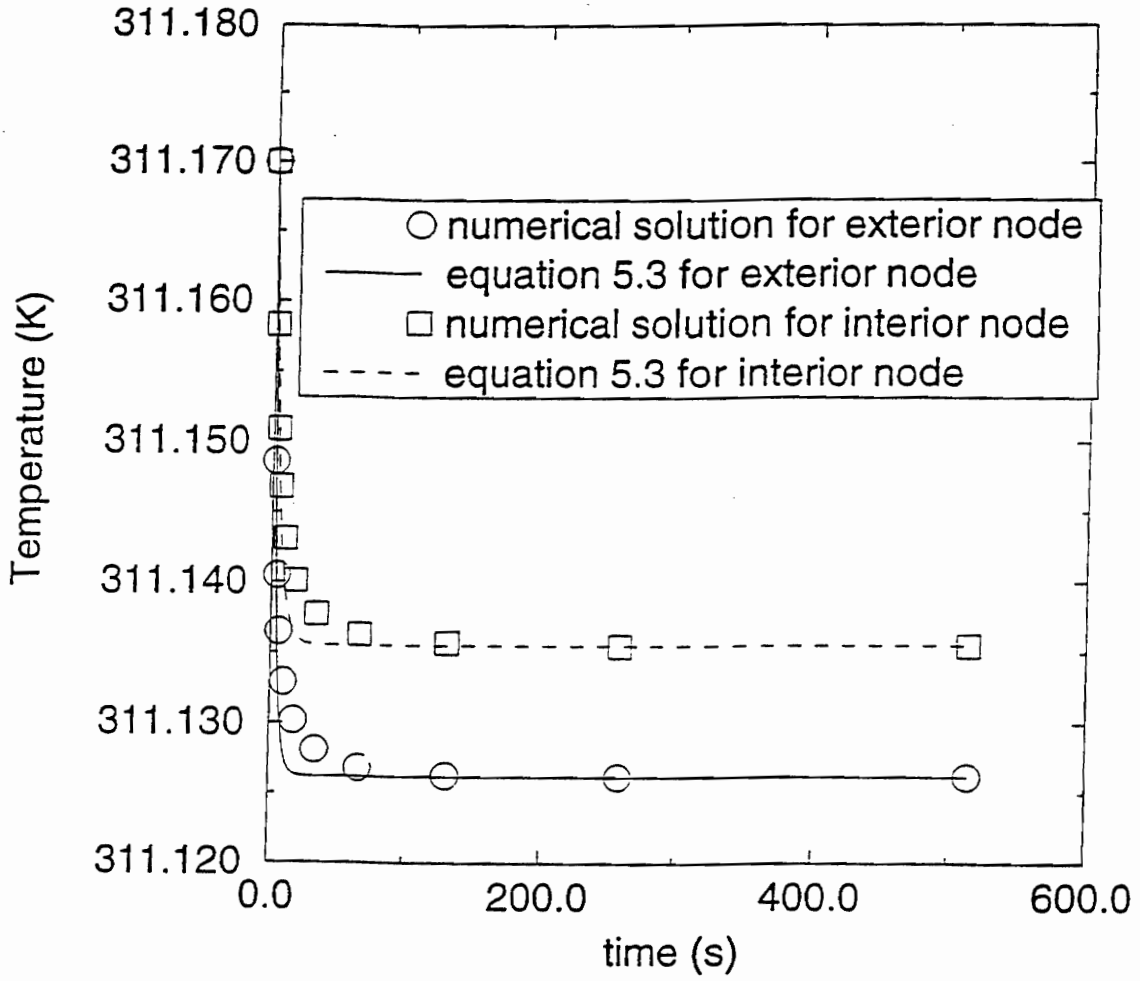

Fig. 20 Transient space-look temperature profiles for an interior and an exterior node on the telescope housing.

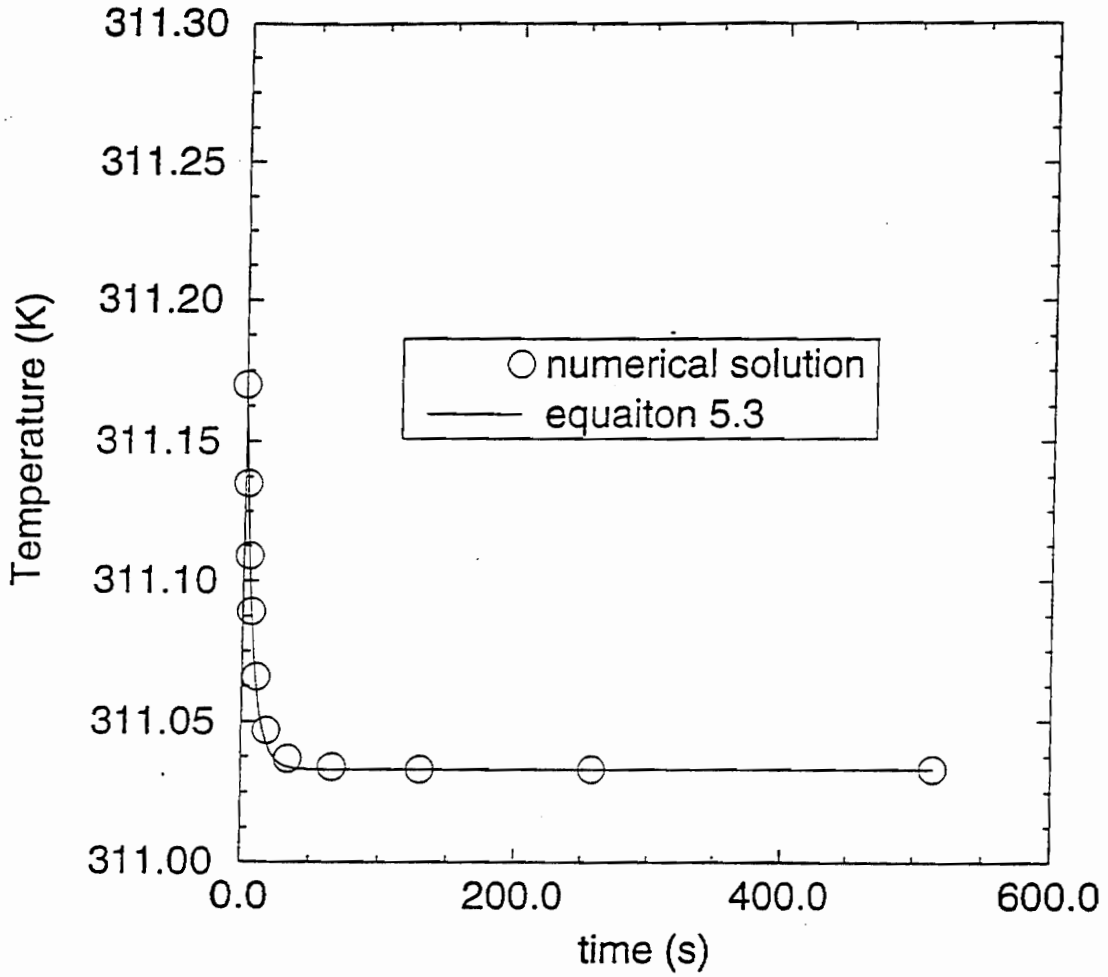

Fig. 21 Transient space-look temperature profile for a node on the secondary mirror mount.

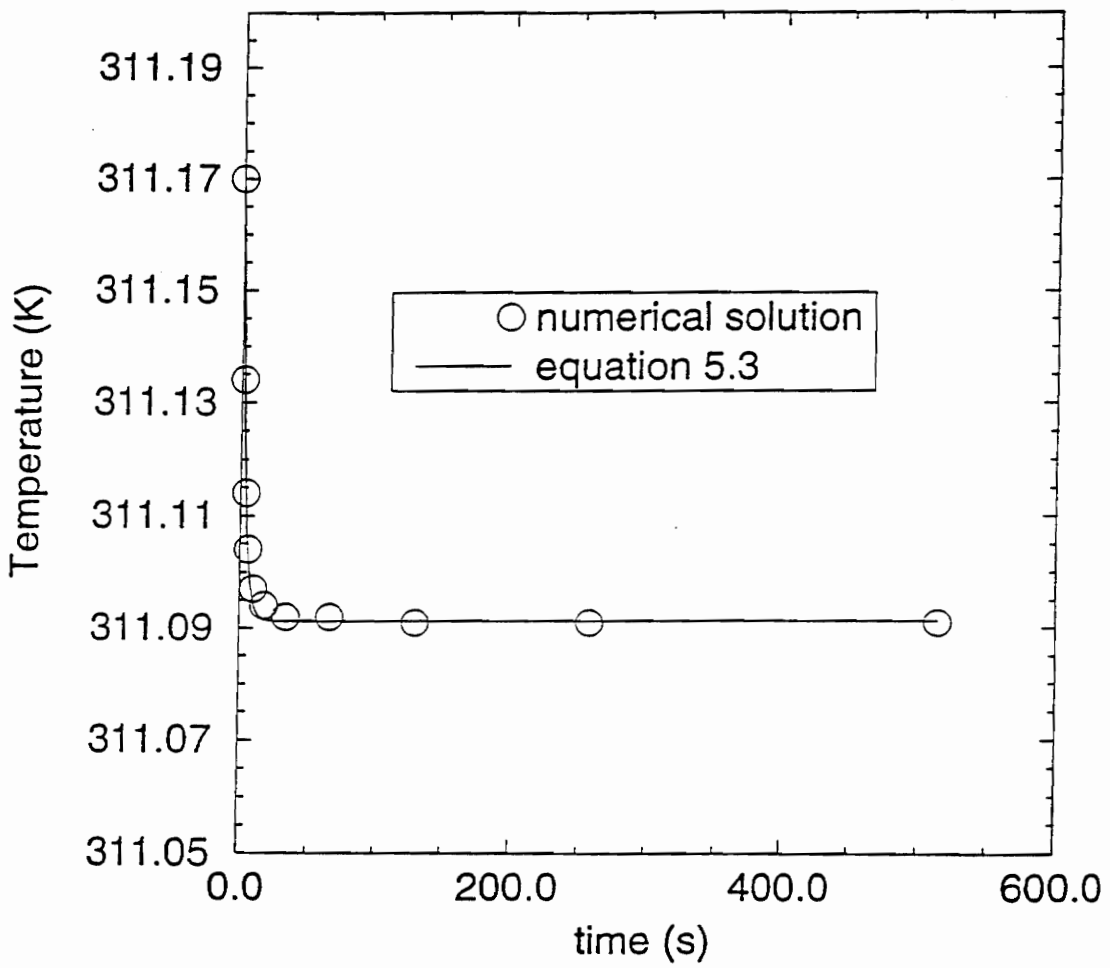

Fig. 22 Transient space-look temperature profile for a node on the reflector cap.

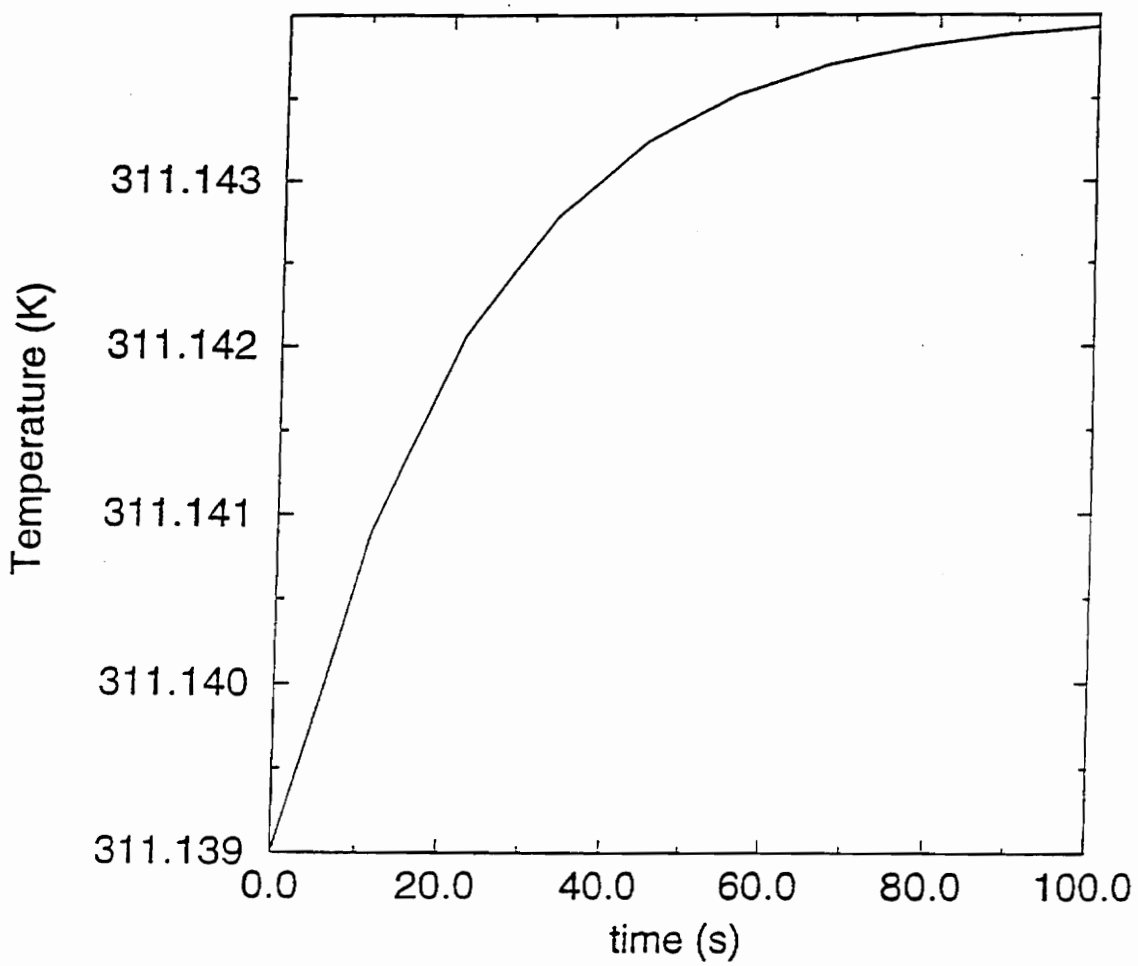

Fig. 23 Transient temperature distribution for a node under the active flake as the instrument scans from a space look to an earth scene.

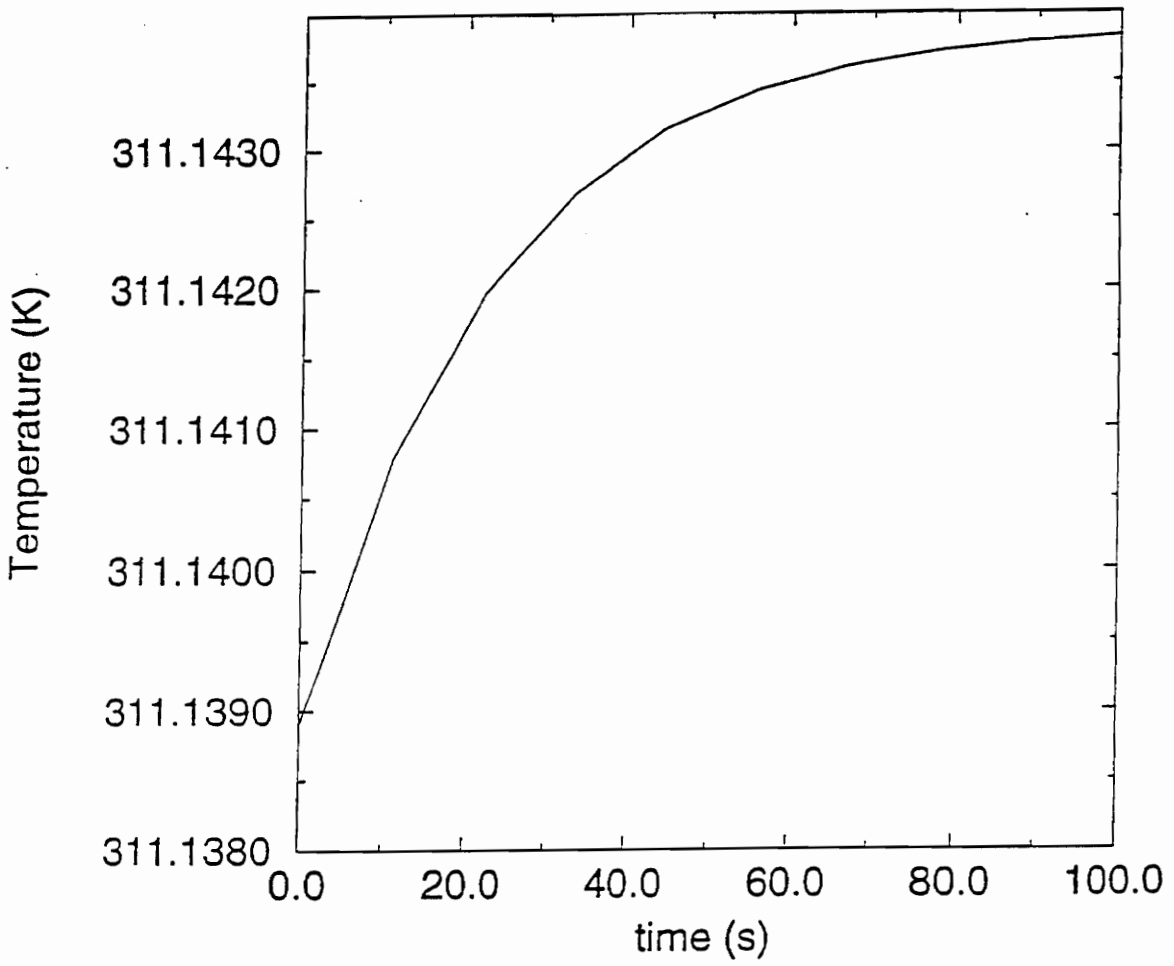

Fig. 24 Transient temperature distribution for a node on the spacer as the instrument scans from a space look to an earth scene.

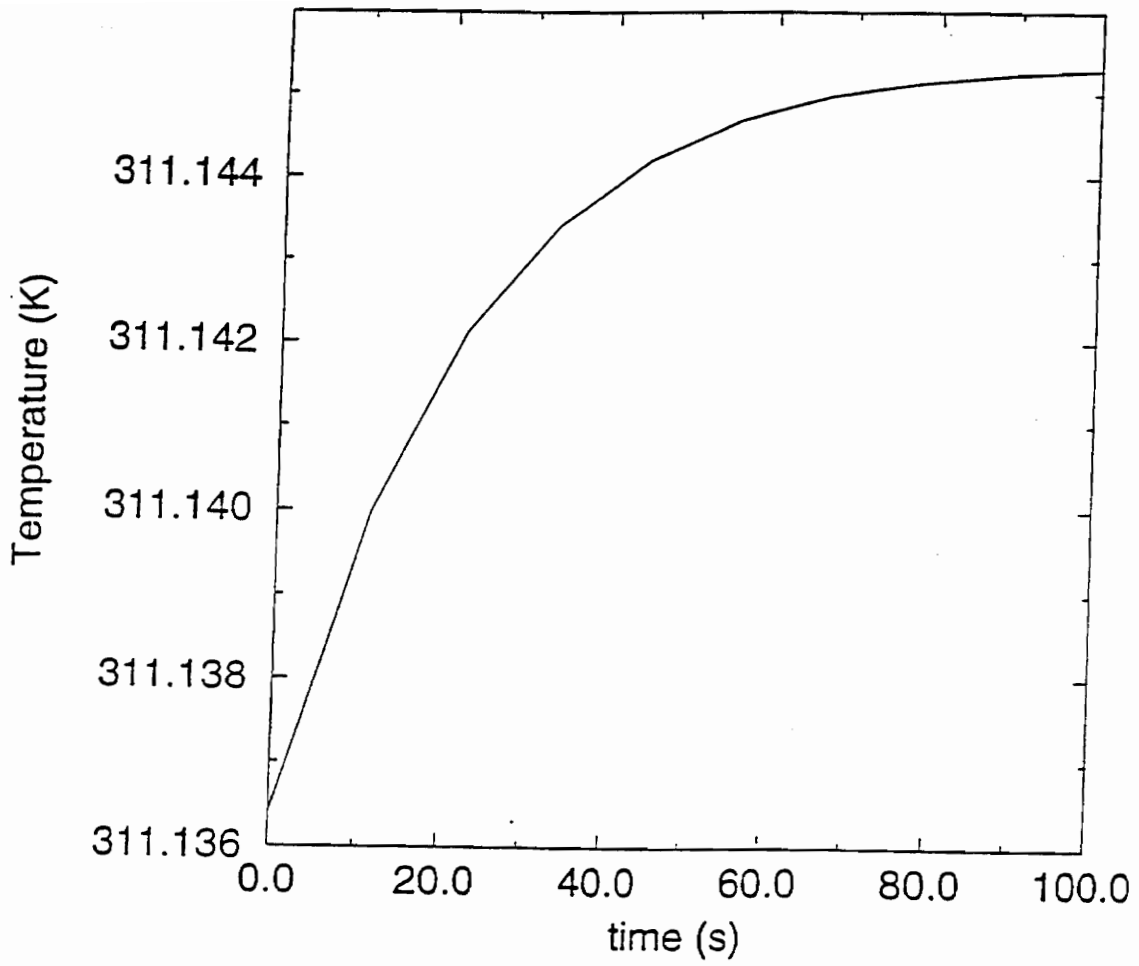

Fig. 25 Transient temperature distribution for a node on the field stop as the instrument scans from a space look to an earth scene.

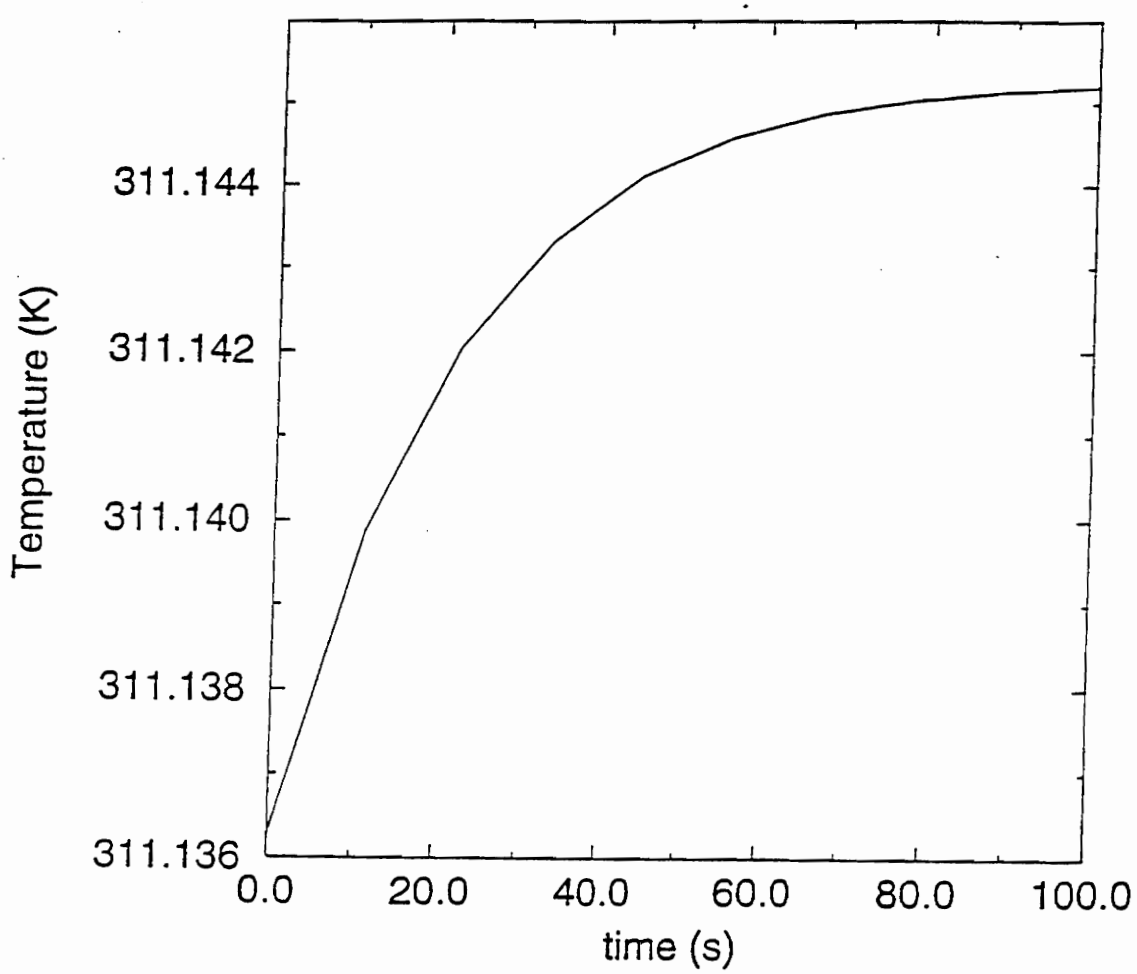

Fig. 26 Transient temperature distribution for a node on the primary insert as the instrument scans from a space look to an earth scene.

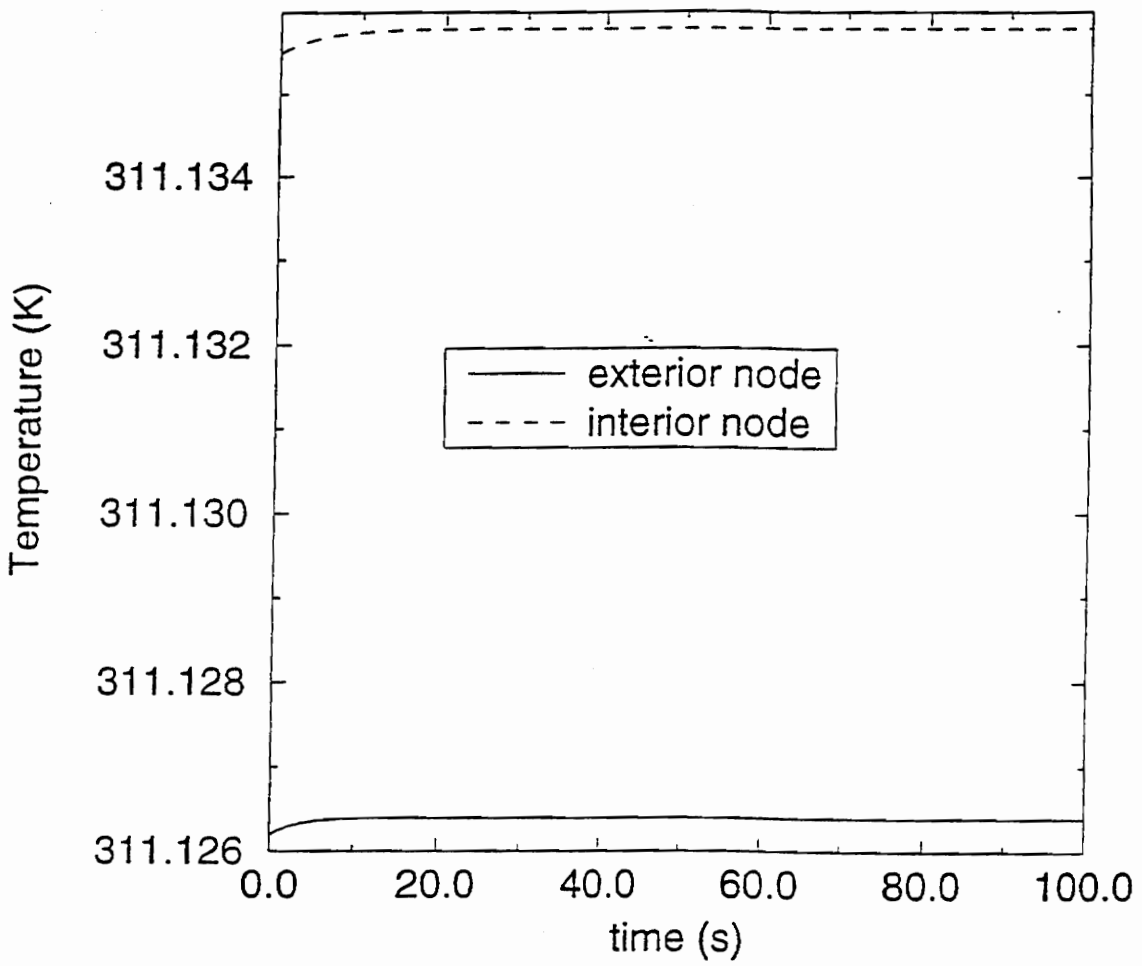

Fig. 27 Transient temperature distributions for an interior and an exterior node on the telescope housing as the instrument scans from a space look to an earth scene.

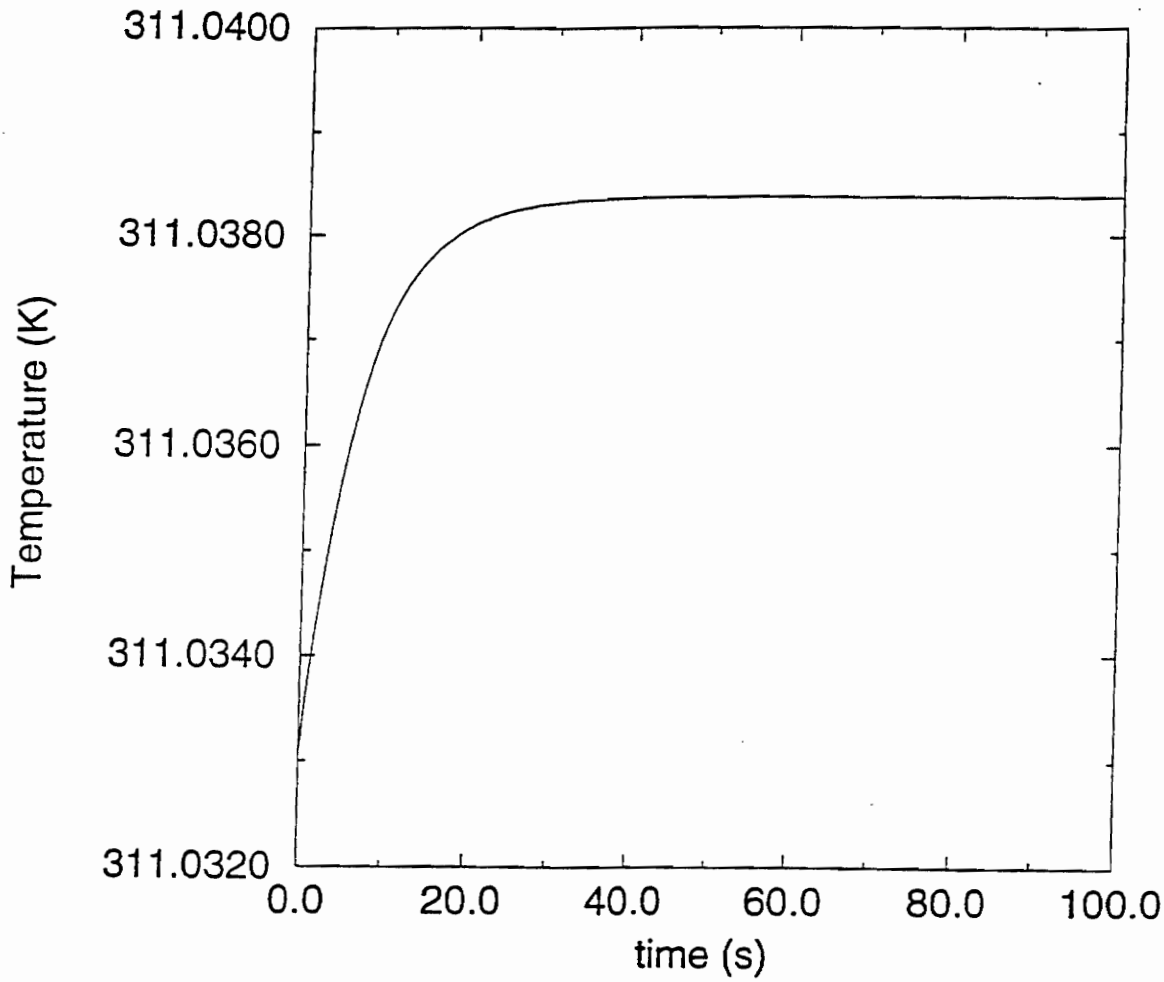

Fig. 28 Transient temperature distribution for a node on the secondary mirror mount as the instrument scans from a space look to an earth scene.

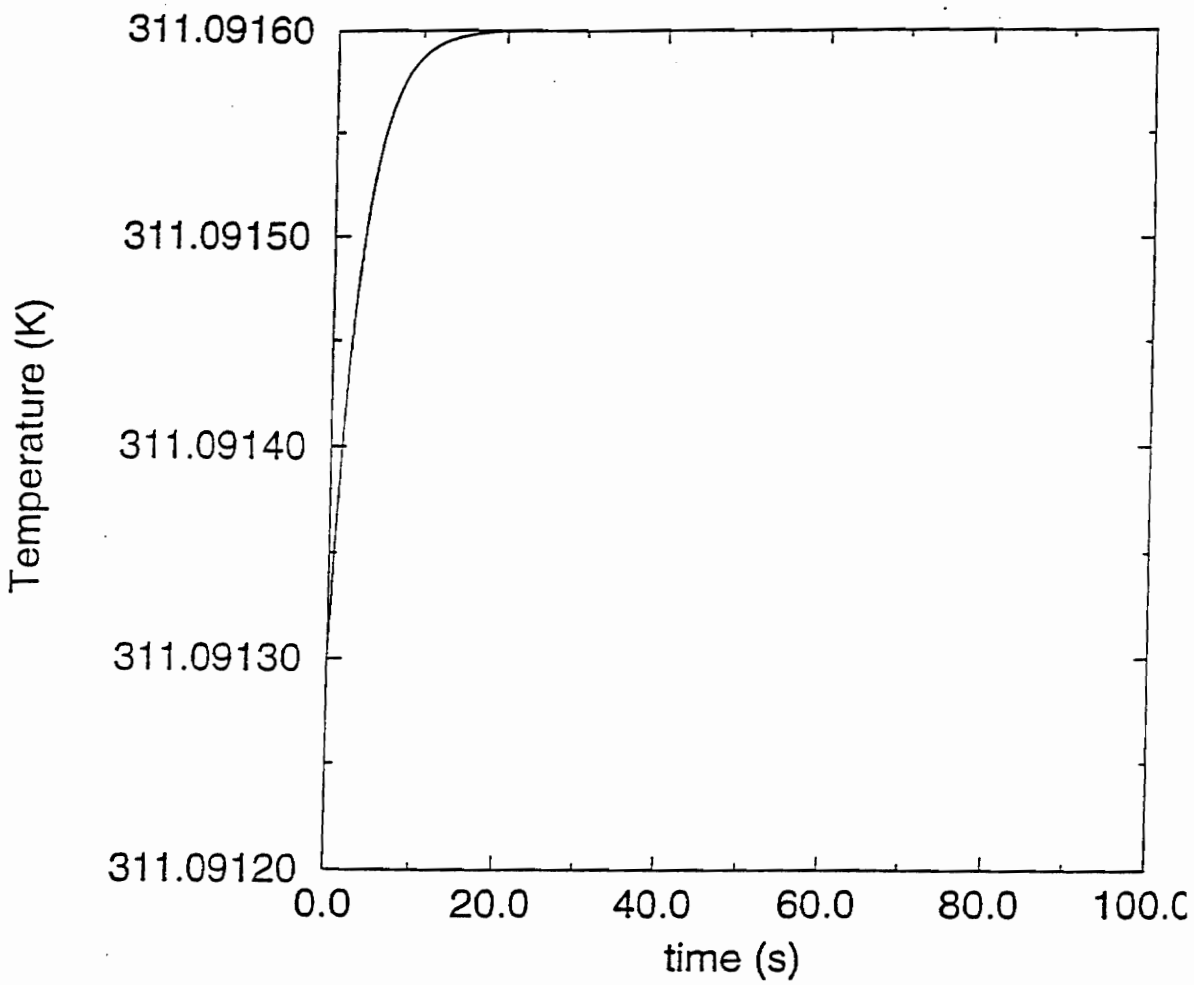

Fig. 29 Transient temperature distribution for a node on the reflector cap as the instrument scans from a space look to an earth scene.

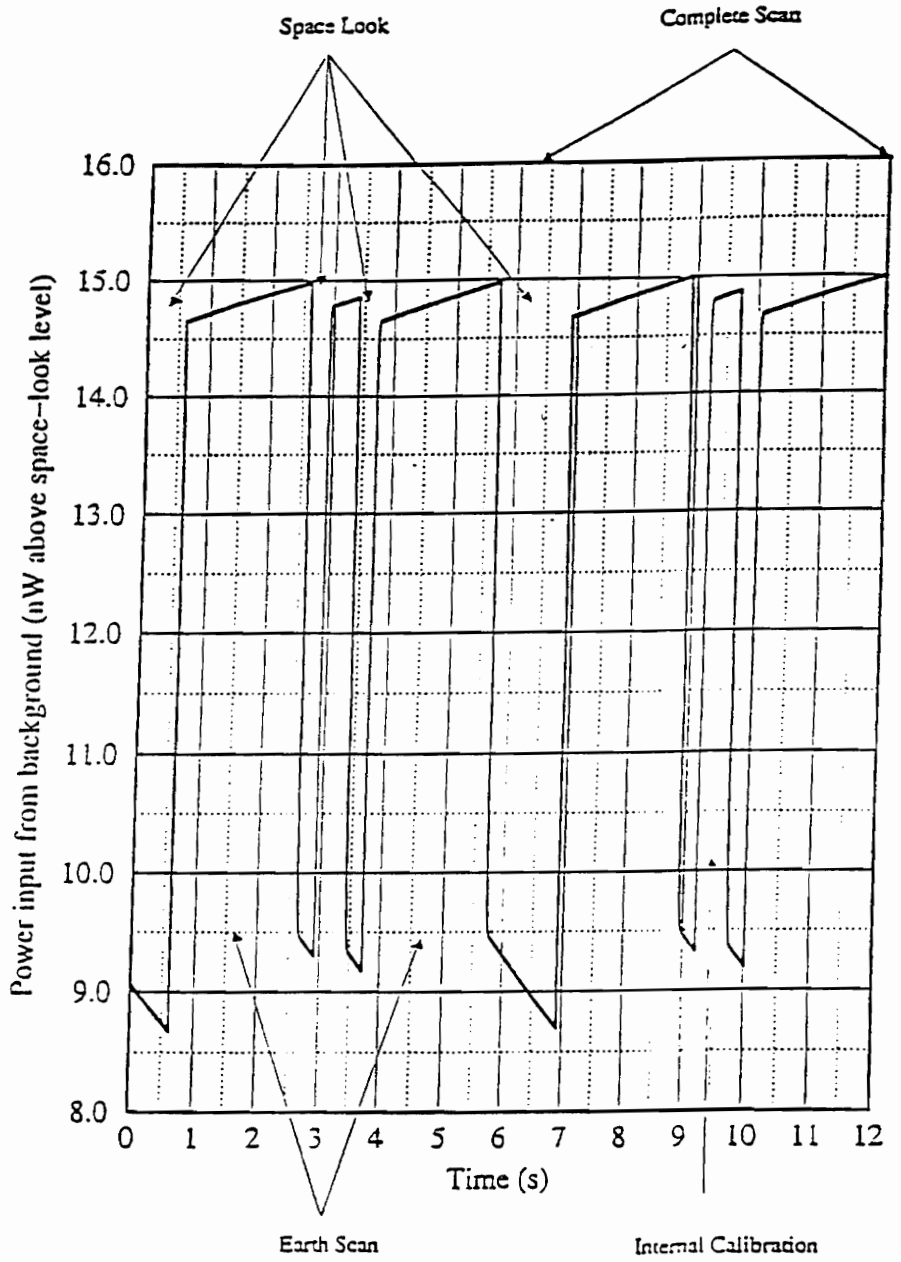

Fig. 30 Transient change in total power on the active flake as the instrument undergoes two complete scans [26].

References

1. Mahan, J. R., Tira, N. E., Lee III, R. B., and Keynton, R. J., *Comparison of the Measured and Predicted Response of the Earth Radiaition Budget Experiment Active Cavity Radiometer During Solar Observations*, **Applied Optics**, Vol. 28, No. 7, April 1989, pp. 1327-1337.
2. Villeneuve, P. V., **A Numerical Study of the Sensitivity of Cloudy-Scene Bidirectional Reflectivity Distribution Functions to Variations in Cloud Parameters**, Ph. D. Dissertation, Department of Mechanical Engineering, Virginia Polytechnic Institute and State University, Blacksburg, VA, (1996).
3. Lee III, R. B., Bolden, W. C., Gibson, M. A., Gibson, M. A., Paden, J., Pandey, D. K., Thomas, S., and Wilson, R. S., *Correlation of Solar Irradiance and Atmospheric Temperature Variations Derived from Spacecraft Radiometry*, **Presented at Step Symposium/5th Cospar Colloquium Johns Hopkins University/Applied Physics Laboratory,** August 24-28, 1992, Laurel, Maryland.
4. Barkstrom, B. R., and Smith, L. G., *The Earth Radiation Budget Experiment: Science and Implementation*, **Reviews of Geophysics**, Vol. 24, No. 2, May 1986, pp. 379-390.
5. Dines, W. H., The heat balance of the atmosphere, Q. J. R. *Meteorol. Soc., 43*, 151-158, 1917.
6. Simpson, G. C., Some studies in terrestrial radiation, *Mem. R. Soc., 2*(16), 69-95, 1928.

7. London, J., A study of the atmospheric heat balance, final report, Res. Div., Coll. of Eng., New York Univ., New York, 1957.

8. House, F. B., Gruber, A., Hunt, G. E., and Mecherikunnel, A. T., *History of Satellite Missions and Measurements of the Earth Radiation Budget (1957-1984)*, **Reviews of Geophysics**, Vol. 24, No. 2, May 1986, pp. 357-377.

9. Kyle, H. L., Hickey, J. R., Ardanuy, P. E., Jacobowitz, H., Arking, A., Campbell, G. G., House, F. B., Maschhoff, R., Smith, L. G., Stowe, L. L., and Vonder Haar, T., *The Nimbus Earth Radiation Budget (ERB) Experiment: 1975 to 1992*, **Bulletin of the American Meteorological Society**, Vol. 74, No. 5, May 1993, pp. 815-830.

10. Barkstrom, B. R., *The Earth Radiation Budget Experiment (ERBE)*, **Bulletin of the American Meteorological Society**, Vol. 65, No. 11, November 1984, pp. 1170-1185.

11. Carman, S. L., Cooper, J. E., Miller, J., Harrison, E. F., and Barkstrom, B. R., *Clouds and the Earth's Radiant Energy System (CERES)*, **Advances in Astronautical Sciences**, Vol. 76, 1992, pp. 693-706.

12. Bongiovi II, R. P., **A Parametric Study of The Radiative and Optical Characteristics of a Scanning Radiometer for Earth Radiation Budget Applications Using the Monte-Carlo Method**, M. S. Thesis, Mechanical Engineering Department, Virginia Polytechnic Institute and State University, Blacksburg, VA (1993).

13. Lee III, R. B., Barkstrom, B. R., Kopia, L. P., Cooper, J. E., Jarecke, P. J., and Folkman, M. A., *The Clouds and the Earth's Radiant Energy System (CERES) Experiment, First Earth Obserbing System (EOS) Instrument*, **Third Annual Space Dynamics Laboratory/Utah State University Symposium on Infrared Radiometric Sensor Calibration**, September 14-17, 1992, Utah State University, Logan, Utah.

14. Fanney II, A. H., **Experimental Study of the LZEEBE Measurement System under Simulated Flight Conditions**, M. S. Thesis, Mechanical Engineering Department, Virginia Polytechnic Institute and State University, Blacksburg, VA (1975).

15. Rasnic, R. L., **A Thermal and Kinematic Model of a Thin-Wall Spherical Shell Satellite**, M. S. Thesis, Mechanical Engineering Department, Virginia Polytechnic Institute and State University, Blacksburg, VA (1975).

16. Passwaters III, J. O., **Detailed Thermal Analysis of a Thin-Shell, Spherical Radiometer in Earth Orbit**, M. S. Thesis, Mechanical Engineering Department, Virginia Polytechnic Institute and State University, Blacksburg, VA, (1976).

17. Eskin, L. D., **Application of the Monte-Carlo Method to the Transient Thermal Modeling of a Diffuse-Specular Radiometer Cavity**, M. S. Thesis, Mechanical Engineering Department, Virginia Polytechnic Institute and State University, Blacksburg, VA, (1981).

18. Gardiner, B. D., **An Analytical Study of Dynamic Response and Nonequivalence of an Absolute Active Cavity Radiometer Operating at Cryogenic Temperatures**, M. S. Thesis, Mechanical Engineering Department, Virginia Polytechnic Institute and State University, Blacksburg, VA (1981).

19. Tira, N. E., **Dynamic Simulation of Solar Calibration of the Total, Earth-Viewing Channel of the Earth Radiation Budget Experiment (ERBE)**, M. S. Thesis, Mechanical Engineering Department, Virginia Polytechnic Institute and State University, Blacksburg, VA, (1987).

20. Tira, N. E., **A Study of the Thermal and Optical Characteristics of Radiometric Channels for the Earth Radiation Budget Applications**, Ph. D. Dissertation, Mechanical Engineering Department, Virginia Polytechnic Institute and State University, Blacksburg, VA (1991).

21. Meekins, J. L., **Optical Analysis of ERBE Scanning Thermistor Bolometer Radiometer Using the Monte-Carlo Method**, M. S. Thesis, Mechanical Engineering Department, Virginia Polytechnic Institute and State University, Blacksburg, VA, (1990).

22. Haeffelin, M. P., **Numerical Study of Equivalence in Scanning Thermistor Bolometer Radiometers for Earth Radiation Budget Applications**, M. S. Thesis, Mechanical Engineering Department, Virginia Polytechnic Institute and State University, Blacksburg, VA (1993).

23. Mahan, J. R., *ME 6324 lecture notes*, Department of Mechanical Engineering, **Virginia Polytechnic Institute and State University**, Blacksburg, VA, 1995.

24. Astheimer, R. W., "*Thermistor Infrared Detectors*", Technical Report, **Barnes Engineering Company,** .

25. Manolo, N., Smith, G. L., and Barkstrom, B. R., *Transfer Function Considerations for the CERES Scanning Radiometer*, **Proceedings of SPIE-The International Society for Optical Engineering**, Vol. 1521, 1991, pp. 106-116.

26. Haeffelin, M. P., **A Study of the Earth Radiation Budget Radiometric Channel Performance and Data Interpretation Protocols**, Ph. D. Dissertation, Department of Mechanical Engineering, Virginia Polytechnic Institute and State University, Blacksburg, VA, (1996).

27. Lee III, R. B., Barkstrom, B. R., Carman, S. L., Cooper, J. E., Folkman, M. A., Jarecke, P. J., Kopia, L. P., and Wielicki, B. A., *The Clouds and Earth's Radiant Energy System (CERES) Experiment, Earth Observing System (EOS) Instrument and calibrations*, **SPIE's International Symposium**, April 12-16, 1993, Orlando, Florida.

28. Carman, S., **CERES Preliminary Design Review**, TRW Space & Technology, Los Angeles, CA, June 23-25, 1992.

29. Incropera F. P., and DeWitt, D. P., *Fundamentals of Heat and Mass Transfer*, Third Edition, **John Wiley and Sons**, 1990.

30. Reddy, J. N., *An Introduction to the Finite Element Method*, Second Edition, **McGraw-Hill, Inc**, 1993.

31. Rey, M., **Heat Conduction Analysis with PATRAN and ABAQUS**, Department of Mechanical Engineering, Virginia Polytechnic Institute and State University, Blacksburg, VA, 1994 (Personal Communication).

32. *PATRAN Plus User Manual, Vol. I*, **Division of PDA Engineering**, 1990.

33. *PATRAN Plus User Manual, Vol. II*, **Division of PDA Engineering**, 1990.

Vita

Max Savransky was born in Ukraine, Kiev, on November 16, 1971. In June, 1979, the whole family arrived in New York City after spending a few weeks in Austria and a couple of months in Italy. In the fall of 1990, Max began his undergraduate studies at the New Jersey Institute of Technology, and in the spring of 1994 he received his Bachelor of Science degree in Mechanical Engineering. In the fall of 1994, Max began his graduate studies at Virginia Polytechnic Institute and State University. He completed his Master of Science degree in December, 1996.

Max Savransky